中央大学博士論文

Multiwavelength Study of Stellar Energetic Flares

Hiroki Kawai

河合　広樹

博士（理学）

中央大学大学院

理工学研究科

物理学専攻

令和３年度

２０２２年３月

CHUO UNIVERSITY

Abstract

Graduate School of Science and Engineering
Physics Course

Doctor of Science

Multiwavelength Study of Stellar Energetic Flares

by Hiroki KAWAI

In 2016, we launched Spectroscopic Chuo-university Astronomical Telescope (SCAT), a telescope capable of visible light spectroscopy, to study stellar flares using Hα emission. SCAT's main stellar flare observations are immediate follow-up observations of stellar flares discovered by the all-sky X-ray monitor, MAXI. We evaluated the performance of SCAT and found that it can observe the Hα line (6563 Å) with a wavelength resolution R of 600 and a limiting magnitude of 13. We operated a follow-up observation system using SCAT for five years. This operation led to the following results. I was responsible for the installation and performance evaluation of the equipment during the start-up of SCAT. I also led the operation of the system, 60% of which was done by the author himself.

We report the results of our simultaneous observations of large stellar flares with soft X-rays (SXRs) and Hα emission line. The energies released in the flares in the SXR and Hα emissions were 10^{36}–10^{38} and 10^{35}–10^{37} erg, respectively. It is rendering the set of the observations to be the first successful simultaneous X-ray/Hα one of the stellar flares with energies above 10^{35} erg. Combining the obtained physical parameters and those in literature for solar and stellar flares, we obtained a good proportional relation between the emitted energies of SXR and Hα emissions for a flare energy range of 10^{24}–10^{38} erg. The ratio of the Hα line emission to that of SXR is about 0.1, if we take the energy band from 0.1 to 100 keV for the X-ray luminosity, in which we integrating the best-fit thin thermal model. We also found that the e-folding times of SXR and Hα light curves, in the decaying phase for a flare, is comparable with the range of 1–10^4 s. Even very large stellar flares with energies of 6 orders of magnitude larger than the most energetic solar flares follow the same scaling relationships established for solar and much less energetic stellar flares. This fact suggests that their physical parameters can be estimated on the basis of the known physics of solar and stellar flares.

Contents

List of Figures

List of Tables

Chapter 1

Introduction

1.1 Solar and Stellar Flares

A stellar flare is a sudden release of magnetic energy that occurs on the stellar atmosphere and is known to radiate light at a variety of wavelengths. Since each wavelength has a different radiative porocess, multi-wavelength observations have been conducted to understand stellar flares. In particular, solar flares, of which the distance is most closest from us, have long been studied as a sample for understanding stellar flares, because they can be observed with high spatial resolution. Based on solar flare observations, the energy release process for stellar flares has generally been considered to be magnetic reconnection (Shibata and Magara, 2011). However, it is still unclear whether other stellar flares are generated by the same mechanism. They have been reported to have energies up to seven orders of magnitude higher than the maximum radiation energy of flares produced by solar flares. Therefore, these flares are a good target for discovering universal correlations using flares of various radiative energies, although they do not provide spatial information directly. Our motivation is to understand what is the stellar flare by using multi-wavelength observation.

Stars that cause stellar flares are not only single stars like the Sun, but also binary systems. In particular, RS CVn type close binary stars, where the binary separation is several times the stellar radius, frequently produce flares with large flare energy (Tsuboi et al., 2016). To explain this peculiar phenomenon, Uchida and Sakurai (1985) proposed the scenario that the magnetic fields of RS CVn-type stars interact with those of two stars due to some factor such as shared magnetic fields between binary stars, and that the process of magnetic field amplification is different from that of single stars (Figure **??**). Furthermore, the flares produced by these may be caused by magnetic reconnection in magnetic loops on a scale that straddles the two stars, forming flare loops that look like they span the binary star. This suggests that flares produced by binary stars may be a completely different phenomenon from solar flares.

1.2 Current flare models based on solar flare observations

Magnetic reconnection is a phenomenon in which magnetic lines of force are reconnected. The conceptual diagram of magnetic reconnection is shown in Figure 1.2. In the shallow part of a low mass star, there is a convection layer. The magnetic field lines penetrating this convection layer are stretched and twisted by the convective motion of the gas and the rotation of the star, and are amplified. The amplified magnetic field is subjected to magnetic buoyancy due to the Parker instability, and rises from the lower part of the convection layer to the surface of the star, where it is

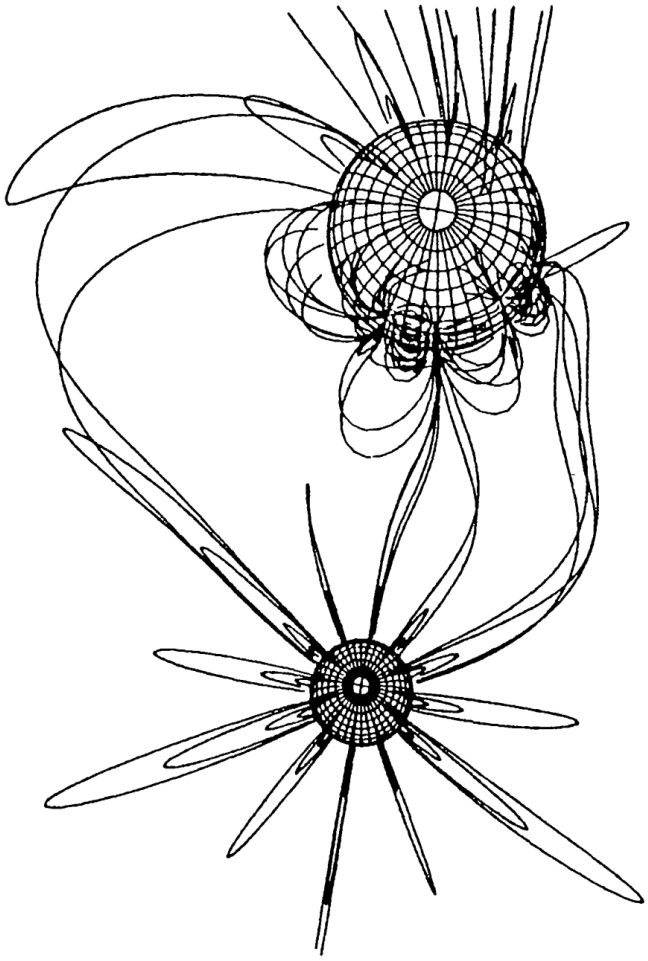

FIGURE 1.1: The schematic image of magnetic loops produced by a binary star.

ejected out of the stellar surface. The ejected magnetic field lines are subjected to the Coriolis force, which causes further twisting. This torsion pushes the magnetic field lines in the opposite direction, and magnetic reconnection occurs.

A schematic diagram of the generation mechanism of Soft X-rays (SXR) and Hα emission in magnetic reconnection is shown in Figure 1.3. Magnetic field lines have a magnetic tension, so when a magnetic field line shaped like a slingshot rubber is formed as a result of reconnection, the plasma frozen by the magnetic field line is accelerated at a furious rate and becomes a reconnection jet. When this reconnection jet collides with the top of the flare loop, a shock wave is generated, the temperature of the plasma reaches 100 million degrees, and hard X-rays (HXR) and SXR are emitted. After that, the accelerated electrons enter the dense chromosphere at the foot of the loop and collide with the ions in the chromosphere. The electrons then collide with the ions in the chromosphere, emitting non-thermal HXR due to bremsstrahlung. This collision converts the kinetic energy into thermal energy and heats up the dense plasma in the chromosphere, causing the excited hydrogen to radiate Hα emission (Hα ribbons). Since the density of the upper part of the chromosphere is 100 times greater than that of the corona, the gas pressure increases remarkably, and a high-density plasma upflow is generated explosively from there

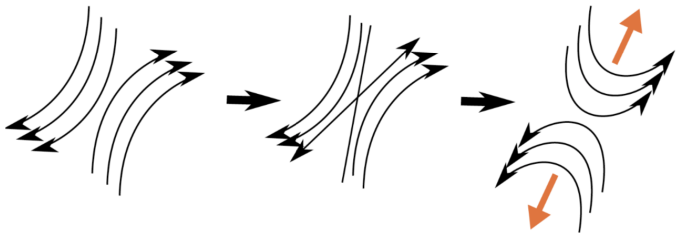

FIGURE 1.2: The schematic images of the magnetic reconnection. A stellar rotation made the antiparallel magnetic field lines. The antiparallel lines are reconnected.

toward the corona. This upward flow is called evaporation flow. This high-density plasma then fills the coronal loop and emits SXR. At this time, the hot plasma at the foot of the loop heats the plasma in the chromosphere by heat conduction and collision of accelerated particles, and the excited hydrogen radiate Hα emission, forming a two ribbon flare (Hα ribbons). Magnetic reconnection occurs many times with each flare, and new flare loops are superimposed on old ones. The old flare loops (post flare loops) are filled with neutral hydrogen, and the Hα line is typically observed as an absorption line. In the case of some high-density ($n > 10^{12}$ cm^{-3}) flares, post flare loops have been observed as emission lines in the Hα line (Svestka, 1976).

1.3 Large stellar flares

Large stellar flares with energies between 10^{34}–10^{39} erg have been detected (**Tsuboi:2016**; Sasaki et al., 2021) with the all-sky X-ray monitor, Monitor of All-sky X-ray Image (MAXI Matsuoka et al., 2009) since its launch in 2009. A majority of the detected flares are estimated to have loop lengths likely larger than the radii of their host stars by a factor of $\sim$5, where to estimate the length they used equations reported by Shibata and Yokoyama (1999) assumed chromospheric evaporation model (Yokoyama and Shibata, 1998), the equilibrium between magnetic pressure and gas pressure and the shape of the flare, a square.Assuming that the shape of the loop of a large flare is the same as that of the sun, the imaginary diagram would look like Figure 1.4. It is unclear whether such giant stellar flares are a different physical process from solar flares. Our motivation is to understand the physical process of giant stellar flares.

The MAXI-detected flares have extremely large energy-related parameters: luminosities of 10^{31-34} erg s^{-1} in the 2–20 keV band, emission measures of 10^{54-57} cm^{-3}, e-folding times of 1 hour to 1.5 days, and total radiative energies of 10^{34-39} erg. **Tsuboi:2016** found a universal correlation between the flare duration and peak X-ray luminosity, combining the X-ray flare data of nearby stars and the Sun (Figure 1.5). Moreover, they found that the MAXI-detected flares extended the established correlation between the flare-peak emission measure and temperature for solar flares and small stellar flares (Shibata and Yokoyama, 1999) (Figure 1.6). Given that the correlations hold over a broad range of energies from solar micro flares to large stellar flares, the correlation suggest the presence of some common mechanism governing flare-loop formation and its cooling processes.

One of the other important observational probe for flare physics is given by the Hα emission. In the solar flare, Hα is known to be emitted from the foot of the loop

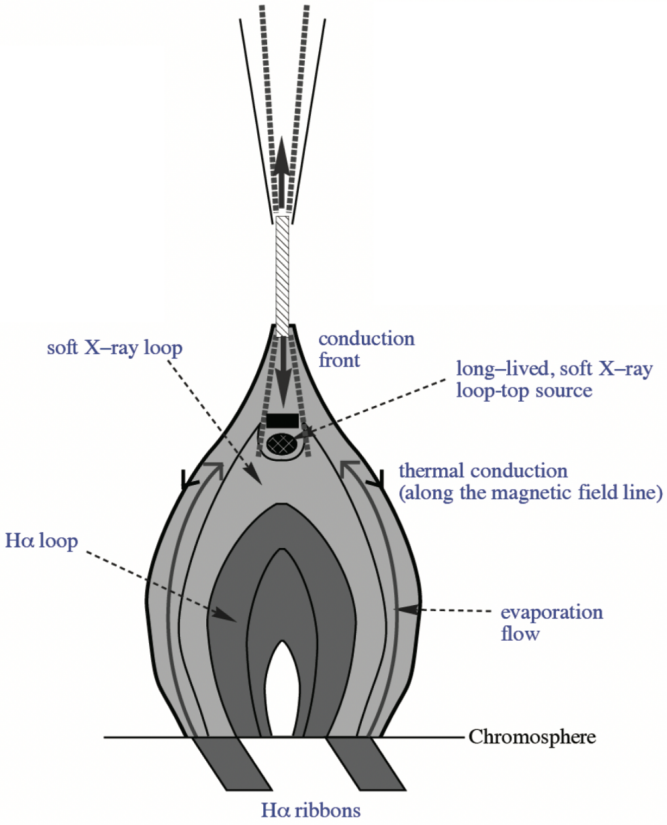

FIGURE 1.3: Magnetic configurations in the flare. The source region of emissions observed in various wavelengths are also presented. See (Shibata and Magara, 2011) for detail.

and/or a flare loop(s) inside the loop that emits soft X-rays (hereafter, SXRs), the former of which is called the "Hα Ribbon". Since the emission region and mechanism are different from those of the SXR, the information obtained from the Hα emission is complementary to that from the SXR emission. Hence, study of the relationship between the SXR and Hα flares from distant stars, where imaging observations are difficult unlike the Sun, can provide key information about the overall geometrical structure and evolution mechanism of stellar flares. Furthermore, by combining the flare loop information from the soft X-ray and the flare foot-point information from the Hα line, we can guess the shape of the stellar flare produced by the binary star.

1.4 Correlations of Stellar flares

Butler, Rodono, and Foing (1988) and Butler (1993) derived a positive relation between the emitted energies with the Hγ emission line and SXR (Figure 1.7). Veronig et al. (2002b) performed a detailed study about solar flares and reported a positive relation between the decay times (e-folding times) of the observed fluxes of the Hα line and SXR (Figure 1.8). However, no studies have been ever conducted about samples containing very large stellar flares, the energy of which can reach orders of magnitude larger than that of the largest solar flares, as those detected with MAXI. Consequently, whereas physics of solar flares is comparatively well understood, our

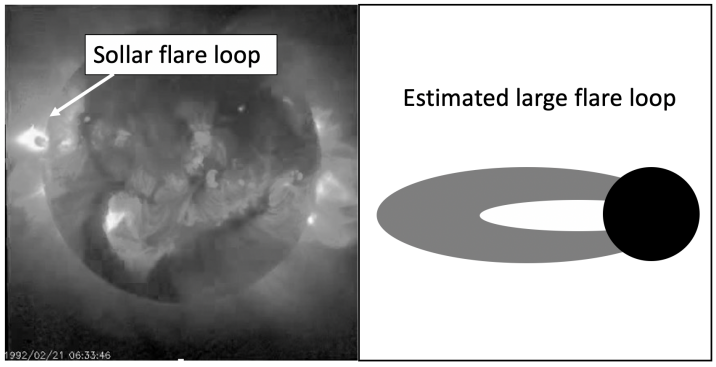

FIGURE 1.4: *Right*: Soft X-ray image of a solar flare taken by Yohkoh. *left*: A schematic view of the estimated large flare loop.

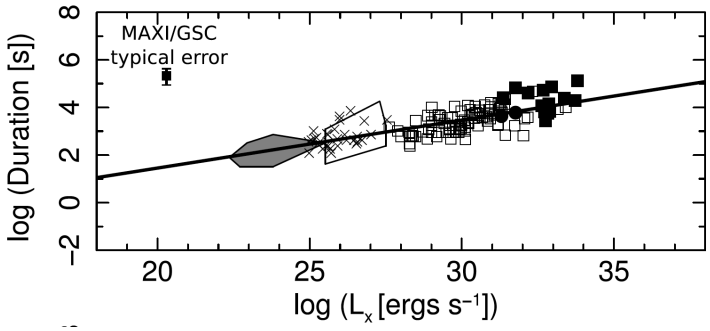

FIGURE 1.5: Universal correlation between duration of flares and X-ray luminosity in the 0.1–100 keV band. The symbols are the same with Figure 1.5. The X-mark and large pentagon are solar flares. See (**Tsuboi:2016**) for detail.

understanding of flare physics of much larger or more active stars than the Sun remains poor and not much more than speculation.

We set up SCAT for Hα observations of giant stellar flares and conducted joint observations with MAXI. In this paper, we first describe the construction of the SCAT system necessary for simultaneous observations in chapter 2. After that, we report the results of our Hα observations (see chapter 2, 3 for the observation details) conducted immediately after triggers of MAXI detection of large stellar flares with emitted energies of up to 10^{38} erg, combining with the simultaneous observations with MAXI (section 3.1) and continuous Hα monitoring. Specifically, we focus on three flares with the best statistics and analyze them in the methods described in section 4.1. These are the first simultaneous observational samples ever reported of the Hα and SXR emissions about stellar flares with energies over 10^{35} erg, which is previous record (a flare from II Peg reported by Butler, 1993). Then we examine the relations about the energy and *e*-folding time between the Hα and SXR emissions and discuss them about spatial information of these flares (section 4.2) before summarizing our result in chapter 5.

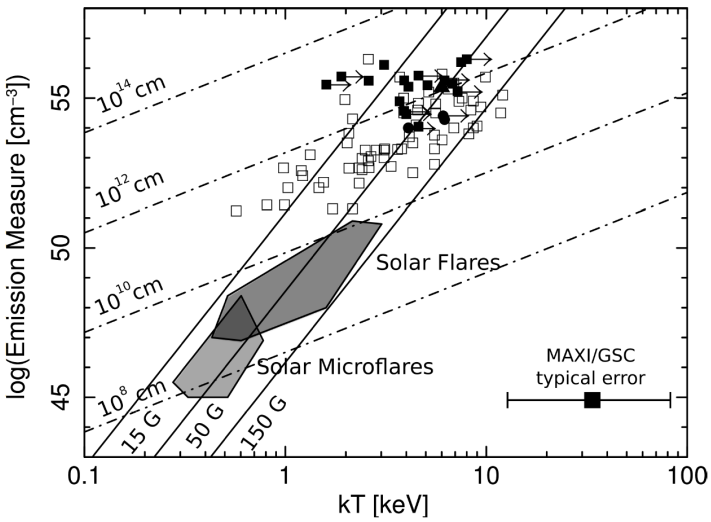

FIGURE 1.6: Universal correlation of emission measure and temperature. Large gray regions express solar flares. The squares, diamonds, circles, and triangles show RS-CVn type stars, Algol, dMe stars, and YSOs, respectively. Filled symbols and open symbols are MAXI flares and other stellar flares, respectively. See (**Tsuboi:2016**) for detail.

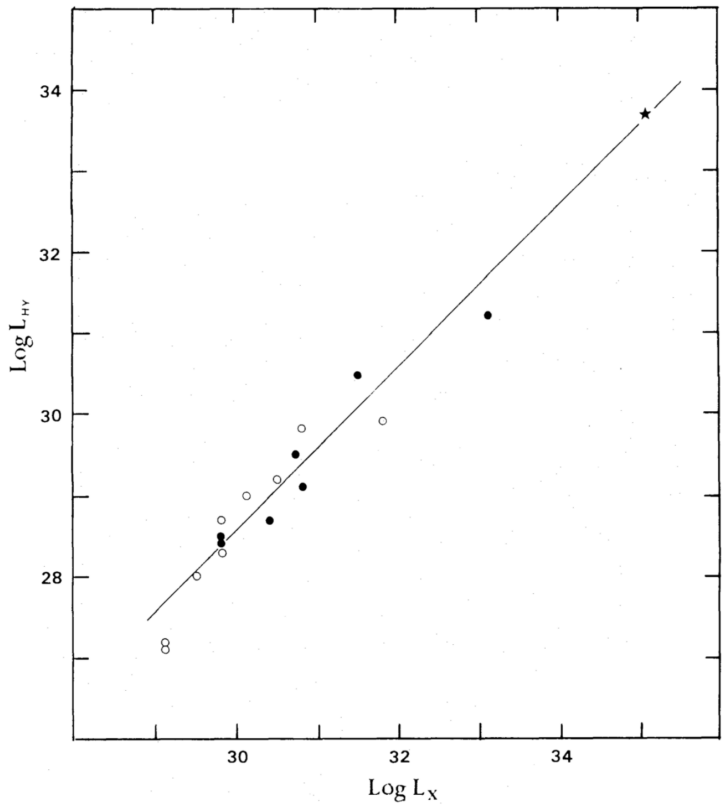

FIGURE 1.7: Universal correlation of radiated energy between Hγ emission and Soft X-ray emission in the 0.04–2 keV band. The star, filled circles and opend circles show RS-CVn type stars, dMe stars and sun, respectively. See (Butler, 1993) for detail.

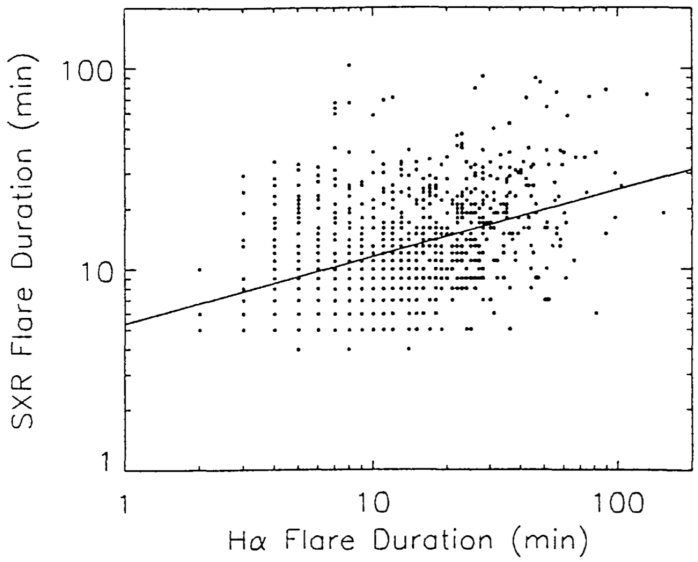

FIGURE 1.8: Universal correlation of duration time between Hα line emission and soft X-ray emission. See (Veronig et al., 2002b) for detail.

Chapter 2

Spectroscopic Chuo-university Astronomical Telescope (SCAT)

In order to observe large flares simultaneously with SXR and the Hα emission, it was necessary to set up an instrument capable of observing the Hα line and executing follow-up observations of flares triggered by MAXI flare detections. We estimated the required performance of SCAT and evaluated whether the launched system has the sufficient performance. I led the construction of these observation systems. In this chapter, we first estimate the required performance. Then we describe the equipment used and evaluate the performance.

2.1 Required performance

First, we summarize the performance requirements of SCAT for ground-based observations of large flares detected by MAXI in the Hα line. Since we capture the time variability of Hα emissions due to flares, we need to obtain stellar spectra with a time resolution of at least 10 minutes and calculate equivalent width (EW) of Hα emission. To measure EW, we only need to know the flux of the emission line component and the flux density of the continuum component, so the low-dispersion specification is sufficient for the wavelength resolution required by SCAT. Then, we set the following conditions: (1) the Hα line must be observable with a low-dispersion performance of a wavelength resolution R of several hundred. In addition, the target object must be brighter than the limiting magnitude to be observed; MAXI has detected stellar flares from 27 stars in its operation (e.g. Sasaki et al., 2017). To confirm the brightness of these sources in visible light, we checked the brightness of each source in the SIMBAD Astronomical Database and drew a histogram (Figure 2.1). As a result, we found that half of the MAXI sources are brighter than 10th magnitude. Therefore, we decided that (2) the limiting magnitude of SCAT should be more than 10 magnitude.

2.2 Instruments

In 2016, we built a SCAT (Figure 2.2, 2.3) on the rooftop of a building on the campus of Chuo University, situated in downtown of Tokyo, Japan (latitude, longitude = 35°42′30″N, 139°44′54″E). Here are the instruments that make up the SCAT. We installed a MEADE 36-cm aperture mirror with a focal length of 2845 mm. We used Takahashi's EM-400 Temma2Z as a mount. As a spectrograph, we mounted a Shelyak Alpy 600, a grism-based spectrograph with a catalog wavelength resolution R of 600 (spectral performance is evaluated in section 2.3). We used an ATIK 460EX CCD camera with a chip size of 12.4 $\times$ 9.98 mm as the sensor for spectral imaging.

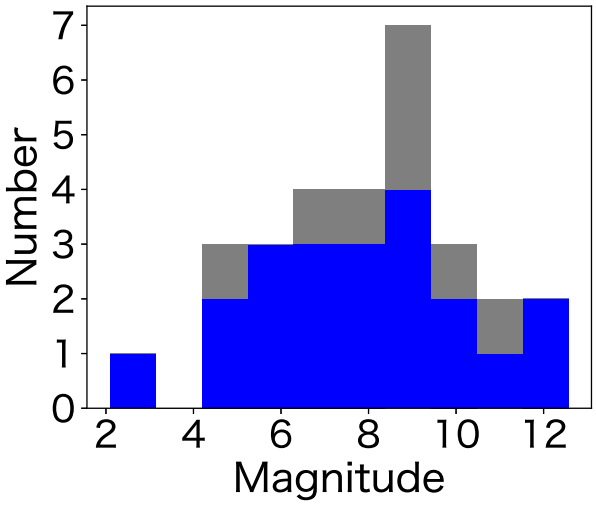

FIGURE 2.1: The histgram of V-band magnitudes of MAXI flare sources. Blue squares are the stars, which exists at an altitude of 30 degrees or higher for at least one hour per day. Gray squares are others.

As a guide camera for putting the target star in the field of view, we installed an ATIK 314L+ CCD camera and a WAT-910HX/RC night vision camera with a field of view of $10 \times 10\,'$ and approximately $1 \times 1\,^{\circ}$, respectively.

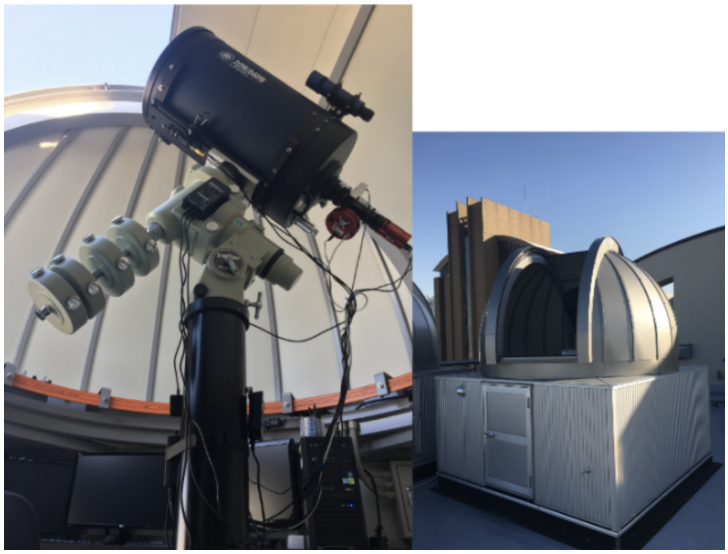

FIGURE 2.2: SCAT overview.

2.3 Performance evaluation

2.3.1 Wavelength resolution and observable wavelengths

To determine the observable wavelength range, we observed the Ar and Ne lamp and UX Ari as a bright source, and drew their spectra using IRAF, a standard analysis software for visible light spectroscopy data (Figure 2.5). In order to determine

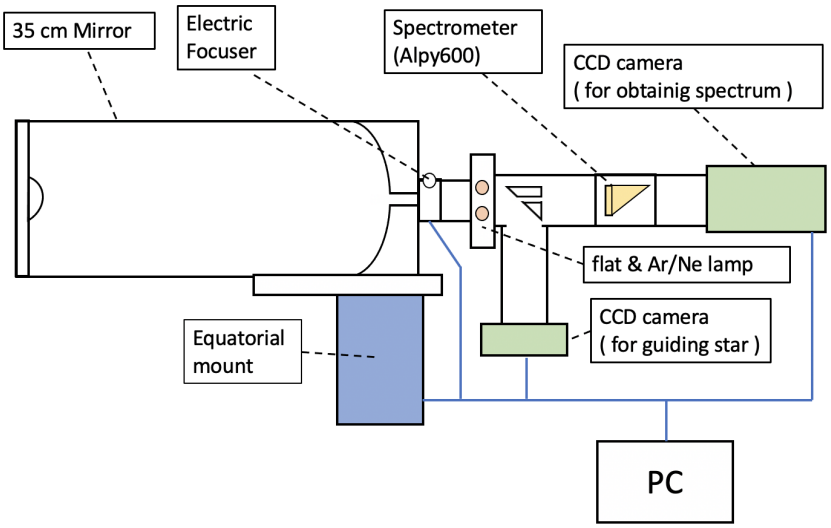

FIGURE 2.3: Side view of SCAT.

FIGURE 2.4: Alpy 600 overview.

the wavelength range where the spectrometer can achieve the catalog value of wavelength resolution R=600, we measured the FWHM of the emission lines identified in the Ar and Ne lamp light spectrum by fitting them with a Gaussian model. The wavelength resolution R was then calculated using the equation $R = \lambda/\Delta\lambda$. The λ is the wavelength at the time of measurement and the $\Delta\lambda$ is the minimum width that can be wavelength resolved. Here, it was set to be the same as FWHM. The FWHMs of each emission line according to its wavelength were drawn in Figure 2.6. The results show that the FWHM is $\sim$10 for most plots at wavelengths below 7500 Å. It means that SCAT has spectral resolution R of 600 at wavelengths below 7500 Å. The data with FWHM greater than 10 in this region were in the form of multiple overlapping emission lines, and the FWHM of only one emission line was $\sim$10. Therefore, we determined that the upper limit of the wavelength interval where the performance of this spectrograph is maintained is 7500 Å. We also checked the spectra of the sources and found that wavelengths below 3700 Å were not detecting enough photons to be statistically significant compared to other wavelengths. These results

indicate that SCAT has the wavelength resolution R of 600 at 6000 Å, and the observable wavelength range is 3700–7500 Å. It satisfies the requirement of (1).

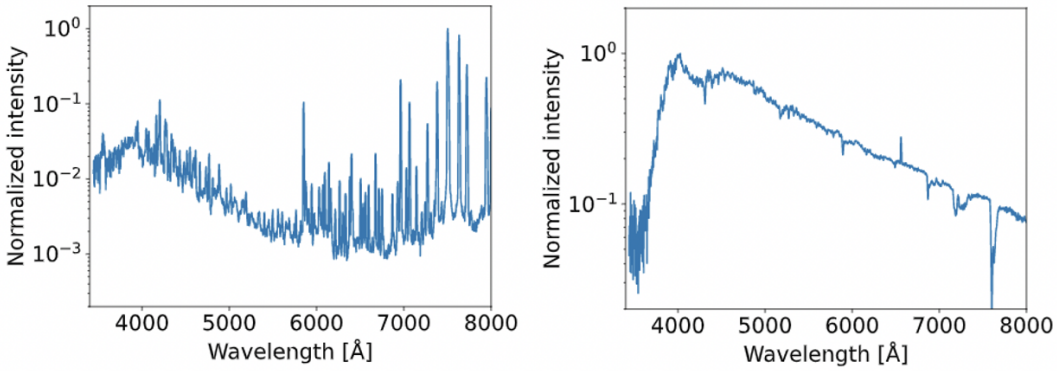

FIGURE 2.5: *Left*: The spectrum of Ar and Ne lamp. *Right*: The spectrum of bright source (UX Ari).

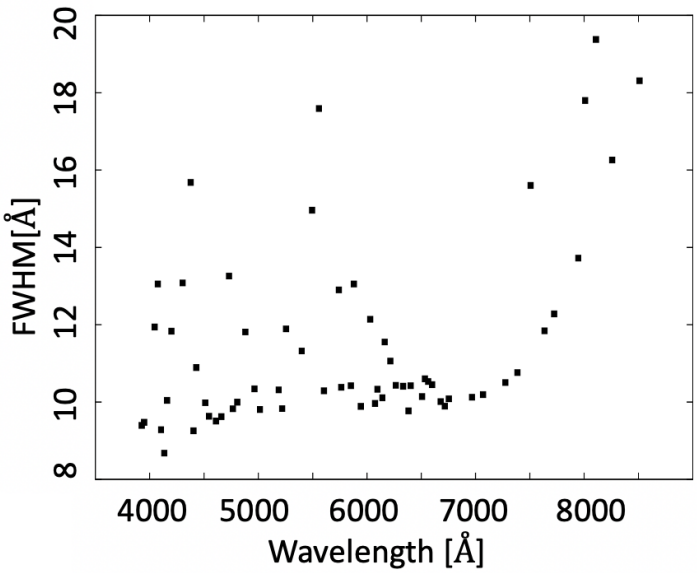

FIGURE 2.6: Correlation between FWHM and wavelength of emission lines in the spectrum of Ar/Ne lamp.

2.3.2 Limiting magnitude

We determined the limiting magnitudes of SCAT by using the method of determining the limiting magnitudes of the guide cameras used to control the telescope's attitude. In order to perform spectroscopic observations with the Alpy 600 at SCAT, the direction of the telescope must be adjusted using the guide camera (ATIK 314L+) so that the star image of the target object is above the slit, which is about 10 arc seconds wide and attached in front of the spectrograph (Figure 2.7). In addition, the direction of the telescope needs to be corrected as the object moves so that the position of the star image is always on the slit during the observation. This correction was done

using the function provided in Artemiscapture, which was used as the imaging software. The frequency of this correction was every second, because empirically, if it is not done every few seconds, the star image and the slit will be misaligned. Therefore, the objects that can be observed with an exposure time of one second with the guide camera are considered to be the limiting magnitudes for SCAT observations. Therefore, we observed objects of various magnitudes to investigate the limit magnitude of the guide camera with the exposure time of 1 second, and determined that it is 13 magnitude. The actual spectrum of Swift J0243.6, a 13th magnitude source, shows a S/N of 60 for 3.3 hours of observation. Therefore, we determined that SCAT has the limiting magnitude at 6000 Å of about 13 magnitude. However, since the time variability of stars on a few hours' scale cannot be determined with observations every 3.3 hours, we decided to focus on objects of magnitude 10 or lower, which can be observed with the same accuracy with a 10-minute exposure time in this work. Since more than half of the stars that MAXI has observed the flare so far have a visible brightness of 10 magnitude or lower. This performance is sufficient to the requirement (2).

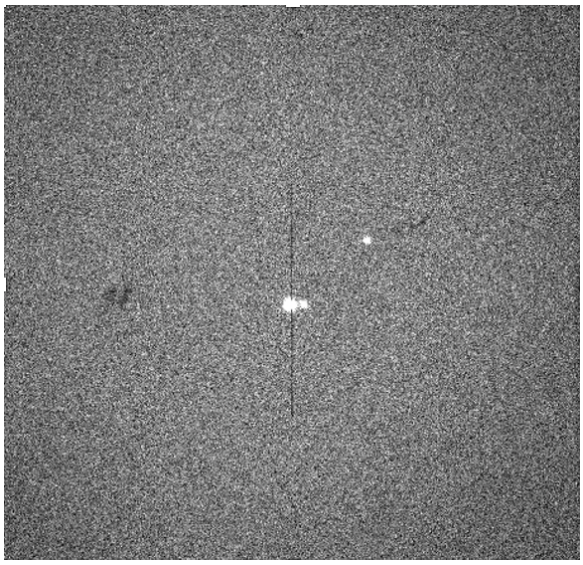

FIGURE 2.7: Photograph observed by the guide camera.

2.3.3 Accuracy of determining the center wavelength

In spectroscopic observations, the component of velocity along the line of sight to the observer can be observed as the Doppler shift of emission or absorption lines. Although we could not observe the Doppler shift associated with Hα flares in this study, the accuracy of wavelength determination is an important parameter to know the information of the source's velocity. In order to determine the accuracy of the wavelength determination, we monitored a source that has been reported to have a periodic Doppler shift due to stellar orbits. We selected the binary system UX Ari (see detail in section 3.4.1), which has a strong emission line in the primary star and a weak absorption line in the secondary star, and a synchronized rotation period of about 6.4 days. The radial velocity fluctuates in a sinusoidal manner with the rotation period, and the profiles of emission and absorption lines appear with an amplitude of about 2 Å. Since the wavelength resolution of our spectrometer is

FWHM=10 Å, it is not possible to separate the UX Ari emission lines from the absorption lines, but we were able to confirm the UX Ari emission lines in the SCAT observation. Therefore, we measured the Doppler shift of the emission line component and checked whether its amplitude was consistent with the literature. We determined the central wavelength of the Hα emission line for all five years of UX Ari data, and folded the temporal variation with the rotation period, and found a sinusoidal variation (Figure 2.8). We measured the amplitude of this variation fitted with a sinusoidal curve was 2 Å, and the 1σ of the variation with the model was $\sim$1 Å. This amplitude is consistent with literature. Therefore, we conclude that it has the performance to determine the absolute wavelength with an accuracy of $\pm$1 Å of SCAT.

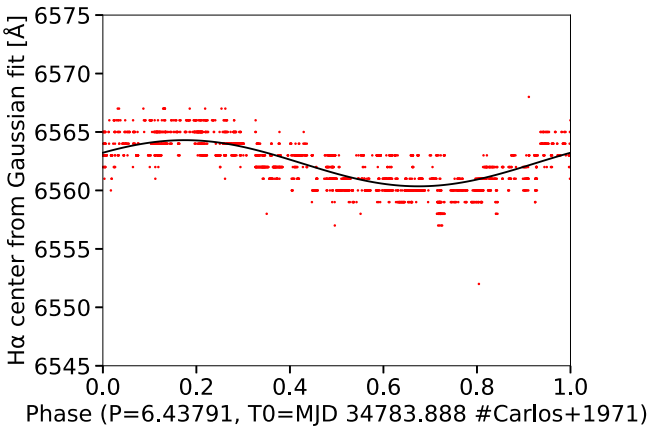

FIGURE 2.8: Phase modulation of center line of Hα emission.

2.4 Simultaneous observation system

2.4.1 Follow-up system

We made use of the “nova alert” system to do a follow-up observation of MAXI-detected stellar flares (Negoro et al., 2016). This automated alert system identifies X-ray transients from the image taken at real time, and classifies them into four type of events; “Burst", “Alert", “Warning", and “Info". While “Burst” is automatically reported to the scientists in the world, “Alert” and “Warning” are examined by duty scientists before reporting. We started follow-up observations with SCAT, just after receiving the signal of “nova alerts” as duty scientists of MAXI..

We started follow-up observations with SCAT, just after receiving the signal of “nova alerts”. We kept SCAT ready for operation on fine nights so that we could make follow-up observations whenever we received the signal of “nova alerts”.

2.4.2 Monitor observation

Apart from the flare periods, SCAT regularly monitored the sources and the data were used to identify their characteristics during the persistent phase. The sources were selected from the MAXI-detected flare sources (e.g. Sasaki et al., 2017).

2.4.3 Rate of the operation

Visible light observations can only be performed when the sky is clear at night. In order to observe more flares in this research, we need to observe every clear day. However, since all SCAT observations are manual, it is difficult to conduct daily observations due to lack of human resources. In this section, I summarize the five-year operation rate of SCAT.

We empirically determined that the sky was clear at night when the sky magnitude was below 16.5. We counted a day as clear at night when the sky magnitude was below 16.5 for more than four hours per day. We show the number of clear days per month over the five years of observations in Figure 2.9. In order to measure the operation rate of monitor and follow-up observations, we also shows the number of days per month that we observed with SCAT by observation team, and by author in Figure 2.9. The observation rate, when observation team mainly conducted observations, was ∼60 %. The author's own observation rate was ∼60 % of the observations made by the observation team. Finally, the total exposure time of the photographs taken by the author during five years of observations was ∼ 63 days.

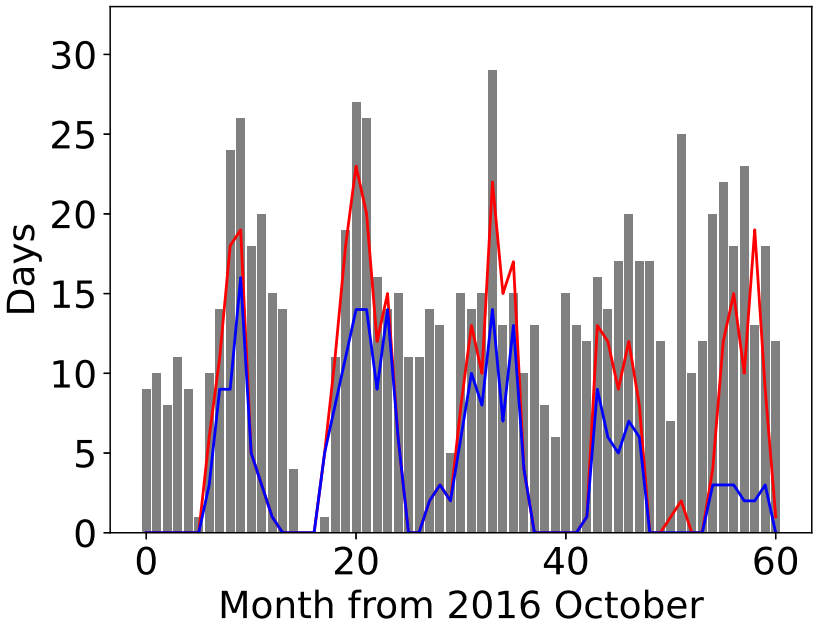

FIGURE 2.9: The gray box shows the number of clear days per month. The red line shows the number of days per month that the observation team made observations with SCAT. The blue line shows the number of days observed by the author himself at SCAT every month.

Chapter 3

Observations

3.1 MAXI

SXR is taken with the Monitor of All-sky X-ray Image, MAXI (Matsuoka et al., 2009). MAXI is an astronomical X-ray observatory mounted on the International Space Station (ISS). In this analysis, we used data from the Gas Slit Camera (Mihara et al., 2011), which is sensitive in the 2–30 keV band. It consists of 12 proportional counters, each of which employs carbon-wire anodes to provide one-dimensional position sensitivity. A pair of counters forms a single camera unit; hence the instrument consists of 6 camera units. The six camera units are assembled into two groups whose field of views (FoVs) are pointed toward the tangential direction of the ISS motion along the earth horizon and the zenith direction. The FoVs are $160^\circ \times 3^\circ$, which corresponds to 2% of the whole sky. These counters are not operated in the regions with high particle background, such as the South Atlantic Anomaly and at absolute latitudes higher than $\sim 40^\circ$, and the vicinity of the Sun (within $\sim 5^\circ$). Hence the Gas Slit Camera has an operating duty ratio of $\sim$ 40% and scans about 85% of the whole sky per orbit of the ISS.

3.2 SCAT

Details of SCAT are given in Chapter 2.

3.3 Simultaneous observations

TABLE 3.1: Time history of our simultaneous observations

Flare ID	Star	Nova alert	SXR peak time	Start time of the SCAT observation
	MJD	MJD	MJD	
Flare 1	UX Ari	57714.1651	57714.2612	57714.4163
Flare 2	UX Ari	58446.7929	58446.7587	58447.4228
Flare 3	AR Psc	58157.9849	58158.0790	58158.3802
Flare 4	UX Ari	58065.6550	–	58065.4675
Flare 5	HR1099	57998.5256	–	57998.6935
Flare 6	HR1099	58158.3790	–	58158.4655
Flare 7	VY Ari	58026.5830	–	58026.6020

We performed follow-up and monitor observations using MAXI and SCAT as shown in Chapter 2, aiming to observe the SXR-Hα emission of large flares simultaneously.

During from 2016 November to 2021 October, we have so far successfully made seven SCAT observations that covered the flare of these MAXI flare-stars. We refer to

the seven flares as Flares 1–7. Flare 1, 2 and 4 occurred at UX Ari. Flare 3 occurred at AR Psc. Flare 5 and 6 occurred at HR1099. Flare 7 occurred at VY Ari. The detection history was listed in Table **??**. All sources detected flare were categorized as RS CVn type close binary star.

3.4 Objects

3.4.1 UX Ari

UX Arietis (UX Ari, HD 21242, HIP 16042) consists of a primary K0 subgiant and a secondary G5 main-sequence star (Fekel, Moffett, and Henry, 1986). The synchronous rotation period is reported to be 6.43788 $\pm$ 0.000007 days (Hummel et al., 2017).

The CHARA six-telescope optical long-baseline array revealed that its spots can fill about 62% of the primary surface (Hummel et al., 2017). Hummel et al., 2017 reported that the radii of the primary and secondary stars are 5.6 $\pm$ 0.1 $R_\odot$and 1.6 $\pm$ 0.2 $R_\odot$, respectively, with an inclination angle of 125.0 $\pm$ 0.5 deg and a separation of 18.8 $\pm$ 0.1 $R_\odot$ (Table 3.2).

UX Ari has been known as a very active flare-star binary (Feldman, 1978; Tsuru et al., 1989; Massi et al., 1998; Massi and Ros, 2002; Catalano et al., 2003; Massi et al., 2005; Peterson et al., 2011). **Tsuboi:2016**, Matsumura et al. (2011). Kawagoe et al. (2014) detected large flares with luminosities of 2 $\times$ 10^{32} erg s^{-1} or larger, using MAXI.

TABLE 3.2: General properties of UX Ari

Parameters	Primary	Secondary	References
Sp. type	K0IV	G5V	(1)
Radius [$R_\odot$]	5.6 $\pm$ 0.1	1.6 $\pm$ 0.2	(2)
Separation [mas]	1.750 $\pm$ 0.01		(2)
[$R_\odot$]	18.8 $\pm$ 0.1		(2)(3)
Distance [pc]	50.2		(3)
Orbital period [d]	6.43788 $\pm$ 0.00007		(2)
Inclination [degree]	125.0 $\pm$ 0.5		(2)

(1)Carlos and Popper (1971), (2)Hummel et al. (2017), (3)ESA (1997)

3.4.2 HR1099

HR1099 (=V711 Taurus) consists of a primary K1 subgiant and G5 main-sequence star with an orbital period of 2.84 days first identified (Bopp and Fekel, 1976). The didtance of 29 pc was observed with HIPPARCOS (ESA, 1997). **Tsuboi:2016**; Suzuki et al. (2010) and Kawai et al. (2017) reported a flare detection by MAXI, revealing a large activity in X-ray flares.

3.4.3 AR Psc

AR Psc (= HD8357 = BD+06 211) consists of a primary K1 subgiant and a secondary G7V dwarf (Fekel, 1996).

The projected rotational velocity ($v \sin i$) of the AR Psc primary is 6.5 ± 2 km s^{-1} whereas the orbital period is 14.3023 days (Fekel, 1996).

AR Psc is an active binary in Hα emission (Fekel, 1996). Fekel, Moffett, and Henry (1986) found that the Hα emission is mostly associated with the component originating from the primary star although that from the secondary has a weak contribution to it as seen in the combined spectrum. AR Psc is also known to be active in the X-ray band (Garcia et al., 1980; Kashyap and Drake, 1999; Shan, Liu, and Gu, 2006). Nakamura et al. (2016) reported a flare detection by MAXI, revealing a large activity in X-ray flares.

3.4.4 VY Ari

VY Arietis (VY Ari, HD 17433, HIP 13118) is known as spectral binary system of spectral type K3-4IVe (Strassmeier and Bopp, 1992). The didtance of 44 pc was observed with HIPPARCOS (ESA, 1997). Since Alekseev and Kozlova (2001) studied the photometric variability of VY Ari, the spotted regions occupy up to 41% of the star ' s total surface.

Kanetou, S. et al. (2015) and Nakamura et al. (2016) reported a flare detection by MAXI, revealing a large activity in X-ray flares.

Chapter 4

X-ray/Hα emission scaling relationships

4.1 Analysis & Results

4.1.1 Light curves & Event selection

The MAXI on-demand system (Nakahira, Ebisawa, and Negoro, 2013) was used to obtain light curves, and spectra. The source photons were extracted from a circular region with a radius of 1°.5 centered on each target, the area of which corresponds to the point-spread function of the detector (Gas Slit Camera) of MAXI. The background photons were extracted from an annular region with inner and outer radii of 1°.5 and 4°.0, respectively, centered at the source position. The resultant curves for the SXR flux was plotted in Figure 4.1, 4.2.

To obtain the equivalent width (EW) of the Hα emission line, we took each frame of the SCAT observations of UX Ari, AR Psc and VY Ari with the exposure of 300 sec, whereas we did that of HR1099 with the exposure of 120 sec. Also, we took the frame of 73 Cet (HD 15318) and 2 Ori (HD 30739) in the same way as the standard stars for photometric corrections. We reduced the SCAT data frame by frame with a standard manner in *python*'s astronomical packages. These reductions are all common among the observations of the flare sources in both flare phases and quiescent phases.

Figure 4.3 shows an example of spectra during flare phase and quiescent phase, but normalized at 6,600Å. We applied a standard technique to our spectra and derived the EW. We fitted the Hα emission line with a Gaussian, and picked up the $\pm 3\sigma$ points from the Gaussian peak as the “edge" between the emission line and continuum emission (Figure 4.3). As for the Hα line intensity, we integrated the data above the linear function which connects the both side of the “edge". As for the continuum level, we took the value of the linear function, just at the center of the Gaussian. We then divided the integrated Hα line intensity by the continuum level, and finally obtained the EW.

Since the targets had orbital variation in EW during the quiescent phase, we needed to determine the curve to subtract the orbital variation. We first folded their light curves, in the quiescent phase, with the rotation period $P_{\rm rot}$, and fitted it with a function of $a \times \sin((x-b)/P_{\rm rot}) + C$, and determined the EW in each orbital phase. Table 4.1 lists the best-fit values of a, b, and C. The value of the EW curve at the same orbital phase was then subtracted from that during the flare and was defined as the EW of the flare. Here, many past optical observations of solar and stellar flares show no large change in continuum flux (e.g. Namekata et al., 2020). We then assume that the continuum flux of our observations does not change from the quiescent to the flare phase. The fact that no significant variation was found for the continuum flux in the band adjacent to the Hff line supports the assumption. As a result, the

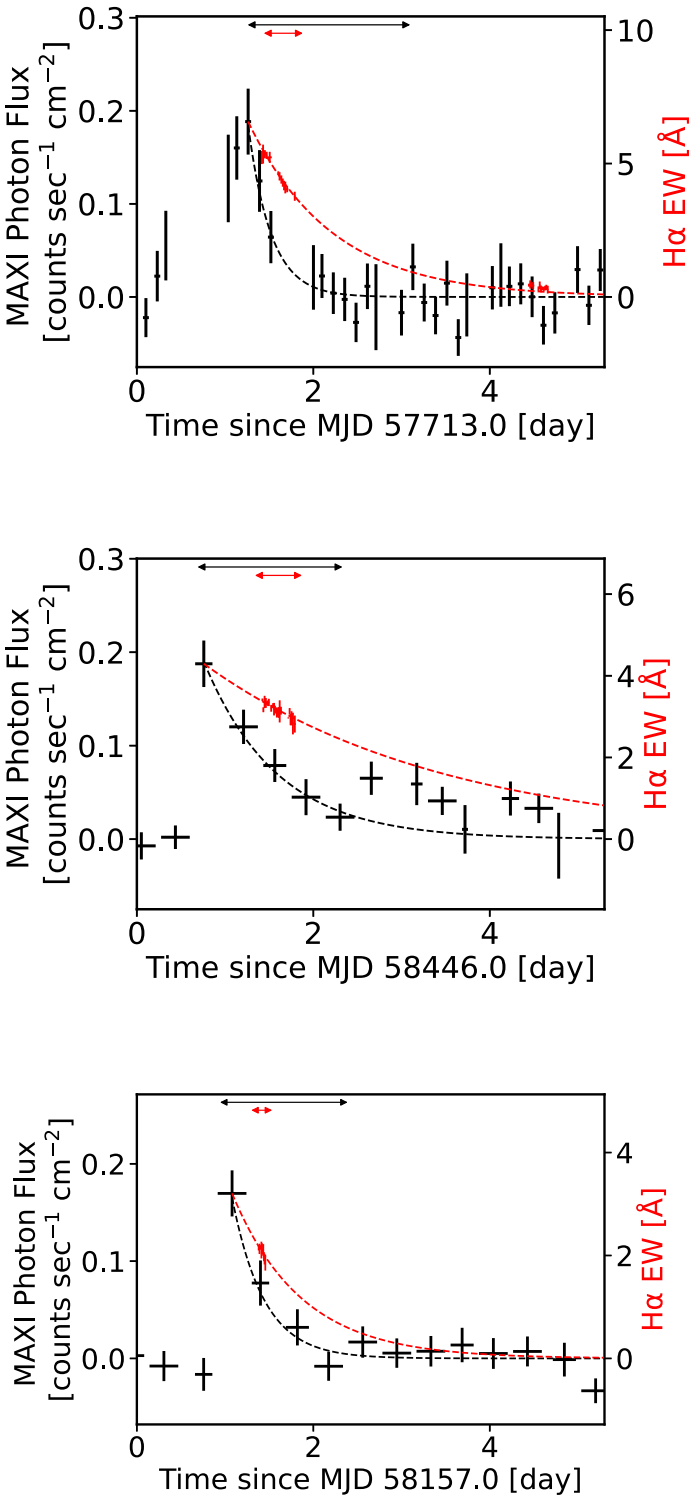

FIGURE 4.1: SXR and Hα light curves of the three of seven flares. The upper, middle, and lower panels correspond to Flares 1, 2, and 3, respectively. The SXR in the 2–10 keV band, overlaid with its best-fit model, is plotted in black, with 1 σ error, with bins for 2, 6, and 6 MAXI orbital periods in the respective three panels. Hα EW is presented in red with 90% error bar for the data and best-fit model. No significant variation is found for the continuum flux in the band adjacent to the Hα line. As a result, the Hα EW is basically proportional to the flux of the band where the line component dominates.

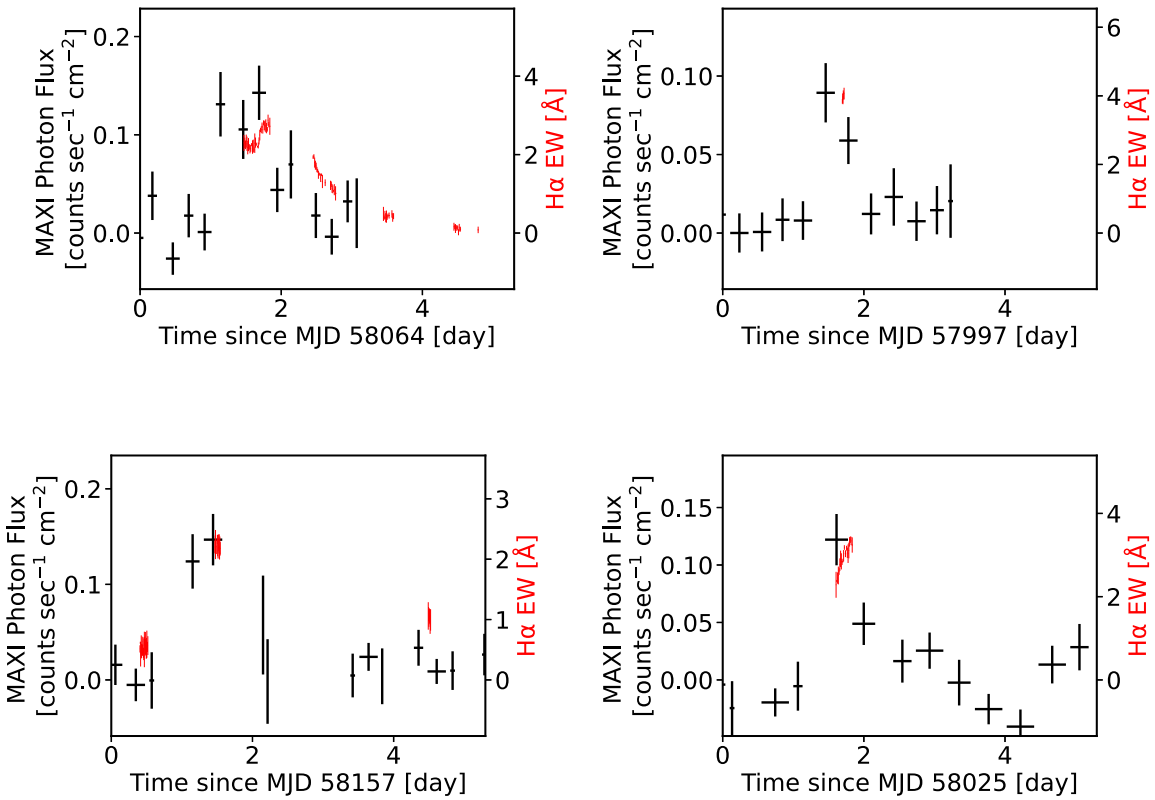

FIGURE 4.2: SXR and Hα light curves of the four of seven flares. The upper left, upper right, lower left and lower right panels correspond to Flares 4, 5, 6, and 7, respectively.

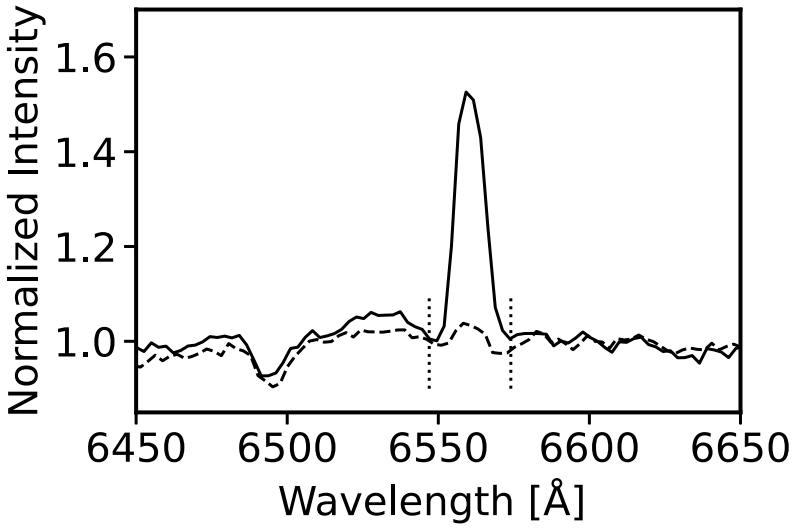

FIGURE 4.3: Normalized spectra in a wavelength range at around the Hα emission line. The solid and dashed lines correspond to Flare 1 and quiescent components, respectively. See text for details.

Hff EW is basically proportional to the flux of the band where the line component dominates. The resultant curves for the EW was plotted in Figure 4.1, 4.2.

TABLE 4.1: EW of Hα during the quiescent phase

Flare ID	Star	Observation dates	a	b	C
Flare 1	UX Ari[a]	2016 Oct – 2017 Mar	1.0	0.8	0.6
Flare 2		2018 Sep – 2019 Apr	0.2	0.0	0.4
Flare 3	AR Psc[c]	2016 Oct – 2017 Feb, 2018 Feb	0.4	0.2	0.1
Flare 4	UX Ari[a]	2017 Sep – 2018 Apr	0.2	0.0	0.4
Flare 5, 6	HR1099[b]	2017 Sep – 2018 Apr	−0.1	0.0	1.1
Flare 7	VY Ari[d]	2016 Oct – 2017 Jan, 2018 Sep, Oct	−0.2	0.2	−0.3

a – UX Ari observation folded with ephemeris MJD = 56237.634 (Hummel et al., 2017).
b – HR1099 observation folded with ephemeris MJD = 42763.409 (Bopp and Fekel, 1976).
c – AR Psc observation folded with ephemeris MJD = 46079.450 (Fekel, 1996).
d – VY Ari observation folded with ephemeris MJD = 46488.52 (Strassmeier and Bopp, 1992).

We selected Flares 1, 2 and 3 from the light curve of Figure 4.1, 4.2 as the flares for which decay times and energies can be determined for both SXR and Hα lines. For Flare 4, the SXR light curve shows that the two flares overlap by roughly 0.5 day. The first flare has no temporal resolution to estimate decay time in the SXR and Hα emission. The second flare is observed simultaneously by SXR and Hα emission, but since the contribution of the first flare cannot be separated, an independent flare duration cannot be determined. Therefore, it was determined that it was not included in the flares for which decay time could be determined. For Flare 5, it was determined that the decay time could not be determined due to the short observation time of the Hα line. Flare 6 was judged to have no decay time because of the missing SXR data after the peak. Flare 7 was judged to be a flare with no confirmed decay time because there was sufficient observation time for both the SXR and Hα lines, but no decay behavior of the Hα line was observed.

From here on, we will focus on Flare 1, 2, and 3, and show the results of the decay time and radiation energy for each SXR and Hα emission.

4.1.2 SXR emission

We fitted the light curves of the decay phase with an exponential model to derive the decay timescale. The time range used for the fitting of each light curve is shown with a black, horizontal arrow in Figure 4.1. In the light curves, Flares 2 and 3 may have the secondary peaks. Then, we fitted the X-ray light curves, limiting the time region for only ∼2 days from the flare peak (see Figure 4.1) to avoid possible contamination by a potential secondary peak, which may appear then. Table 4.2 lists the fitting results, including the *e*-folding time, τ.

The source spectrum during each flare was extracted from the data of the time bin for the peak flux in each flare (Figure 4.1) and background component, accumulated from the above-mentioned annular region, is subtracted from it. The latter represents the sum of the instrumental and sky background components. Figure 4.4 shows the resultant flare spectra. Although the spectra contain the quiescent component, the contribution is negligible; Webb et al. (2020) presented the catalog of active stars, including our targets, UX Ari and AR Pic, which contains the quiescent fluxes

TABLE 4.2: Flare e-folding time τ

Flare ID		Region of interest [d] / [10^4 s]	τ [10^4 s]	Reduced χ^2 (d.o.f.)
Flare 1	SXR	1.9 / 16	2 (1–4)	0.3 (9)
	Hα	0.5 / 4.3	8 (7–10)	0.6 (11)
Flare 2	SXR	1.9 / 16	7 (5–10)	0.2 (3)
	Hα	0.4 / 3.5	24 (19–32)	0.8 (22)
Flare 3	SXR	1.5 / 13	3 (2–5)	0.8 (2)
	Hα	0.08 / 0.69	7 (4–17)	0.4 (8)

Note – d.o.f. means the degree of freedom. In the 2–10 keV band for SXR. The errors are 90% confidence range.

of the sources. Their flux levels are about 3% or lower of any peak fluxes of the flares we reported here.

We fitted the spectra with a thin thermal plasma model, APEC (Smith et al., 2001) in the Xspec package, where the redshift and metal abundace were fixed to zero and 0.3, respectively. In the fitting, as for Flares 1 and 2, we fixed the temperature kT to the average value according to **Tsuboi:2016** because otherwise no meaning constraints would be obtained due to poor data statistics. Table 4.3 lists the fitting results and Figure 4.4 shows the best-fit models. Then, the radiation energies were calculated, from the best-fit e-folding timescale and the luminosity, and are given in Table 4.4.

TABLE 4.3: SXR best-fit spectral parameters

Flare ID	kT [keV]	Emission measure [10^{55} cm^{-3}]	Reduced χ^2 (d.o.f.)
Flare 1	3.5[a]	5 (3–6)	0.1 (4)
Flare 2	3.5[a]	4 (3–5)	1.7 (8)
Flare 3	3 (2–6)	4 (3–7)	0.8 (6)

Note – d.o.f. means the degree of freedom. Abundance and redshift are fixed to 0.3 and 0, respectively. The errors indicate a 90% confidence range.
a: kT is fixed according to **Tsuboi:2016** (see text for detail).

TABLE 4.4: Summary of the three flares

Flare ID	Star	Flare peak time UT	Flare peak time MJD	Wavelength	Peak luminosity [10^{32} erg s^{-1}]	Energy [10^{36} erg]
Flare 1	UX Ari	2016/11/22 06:16	57714.2612	SXR	3 (2–4)	6 (2–12)
				Hα	0.13 (0.06–0.20)	1.1 (0.5–1.7)
Flare 2	UX Ari	2018/11/24 18:12	58446.7587	SXR	3 (2–4)	20 (10–30)
				Hα	0.08 (0.04–0.12)	1.9 (0.9–3.0)
Flare 3	AR Psc	2018/02/09 01:53	58158.0790	SXR	2.5 (1.4–3.1)	8 (3–13)
				Hα	0.04 (0.02–0.07)	0.3 (0.1–0.8)

Note – In the 2–10 keV band for SXR. The errors are 90% confidence range. The Hα luminosities represent the values extrapolated to the times of the X-ray peak times. The errors for the Hα luminosities and radiated energies include the uncertainties in determining the decay times.

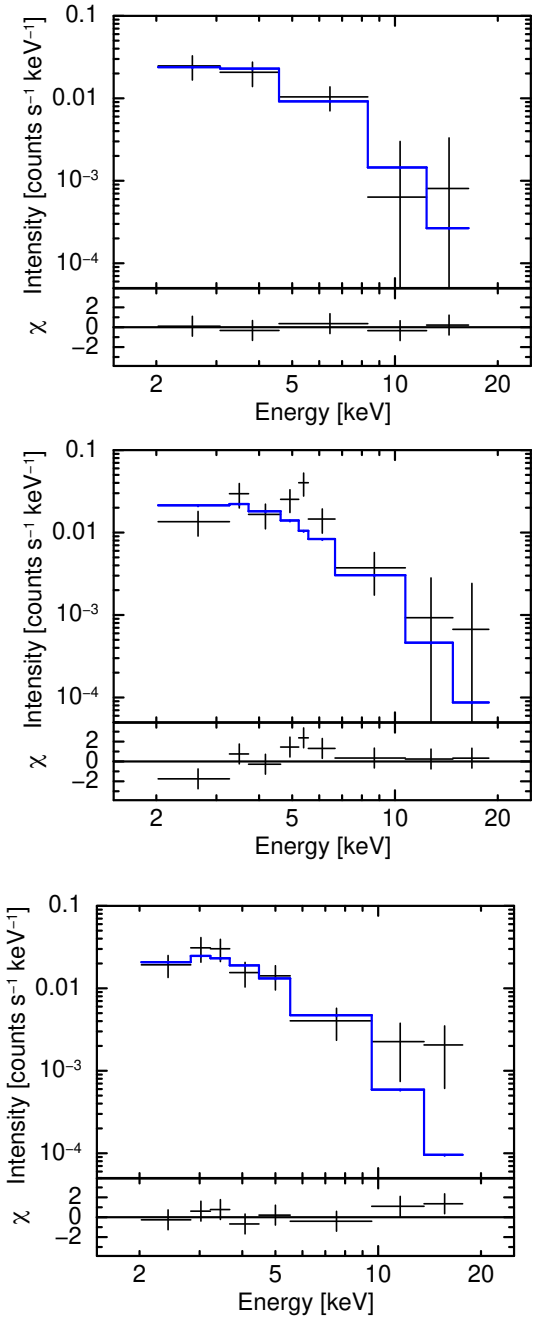

FIGURE 4.4: SXR spectra of Flare 1 (upper panels), Flare 2 (middle), and Flare 3 (lower). The data points are binned for 2, 6, and 6 MAXI orbits in the respective panels. The errors are in 1-σ. The solid lines show the best-fit models. The residuals for the best-fit model are also shown at the lower part of each panel.

4.1.3 Hα emission

We fitted the Hα light curves with an exponential function in the same manner for the SXR light curves. The fitting result is listed in Table 4.2. Here, as for the Hα light curve of Flare 1, we performed fitting for the time region of the first day of the flare peak only, during which an enhancement in emission was apparent. We note that the inclusion of the data in the second observation period (on the fourth day) in the fitting yielded the best-fit decay time of 9.9 (9.5–10.4) $\times 10^4$ s, which is not significantly different from the original result of 8 (7–10) $\times 10^4$ s (Table 4.2); in other words, the selection of the time region between the two for the fitting makes no significant influence on the result.

In order to obtain the released energy during a flare as the Hα line emission, we needed to estimate the peak Hα intensities, although they are not covered in our follow-up observations. Then, we needed to extrapolate the best-fit function to the flare-peak epoch obtained in SXR light curve. We note that it should be a reasonable assumption, given that the coincidence of the SXR and Hα peaks have been reported from the data of roughly 200 solar flares (Veronig et al., 2002a) and also from stellar flares (Doyle et al., 1988a; Fuhrmeister et al., 2011; Namekata et al., 2020).

We calculated the Hα peak luminosity by extrapolating the time-profile of the obtained Hα EW to the X-ray peak time, subtracting the averaged continuum level during one-night observation, and using the distance to the object. The absolute flux measurements of continuum emission is in general known to be very difficult for the spectroscopic data as we took. The continuum level of our data was actually fluctuated in 50% at 90% error. We then gave this error to the Hα flux of our measurements. Table 4.4 shows the results, where the uncertainties in determining the decay times are taken into account in the calculation of the errors.

4.1.4 Flare loop

We determined loop lengths of flares, using the "kT-EM diagram" model formulated by Shibata and Yokoyama (1999), where the pre-flare electron density was assumed to be 10^9 cm^{-3}. Independently, we also derived the same parameters, using the model formulated by Haisch (1983). This model estimates the loop parameters by assuming that the time taken for radiative cooling and conduction cooling are the same and that the cross section of the loop is $(L/10)^2$, where L is the flare loop length. The estimated loop lengths based on the former model were roughly three times larger than the binary separation for Flares 1 and 2, whereas those based on the latter model are comparable to the binary separation. Table 4.5 summarizes the result.

TABLE 4.5: Loop lengths of the three flares

Flare ID	Loop lengths			
	(Shibata and Yokoyama, 1999)		(Haisch, 1983)	
	[$R_\odot$]	(Binary separation)	[$R_\odot$]	(Binary separation)
Flare 1	62 (51–74)	3.3 (2.7–3.9)	11 (7–16)	0.6 (0.4–0.9)
Flare 2	57 (50–67)	3.1 (2.7–3.6)	25 (20–32)	1.3 (1.1–1.7)
Flare 3	80 (30–220)	–	14 (10–19)	–

Note – The errors indicate the 90% confidence range.

4.1.5 Radiation energy

Butler, Rodono, and Foing (1988) presented the linear relationship between the radiation energy of flares in the Hγ emission line ($E_{\mathrm{H}\gamma}$) and that in the X-ray band in the 0.04–2 keV band. Butler (1993) further extended the relation in energy to the range of seven orders of magnitude: 10^{29}–10^{36} erg [1]

In Figure 4.5, we plotted the same kind of the plot; the radiation energy of flares in the Hα emission line ($E_{\mathrm{H}\alpha}$) vs. that in the X-ray bolometric band (E_{Xbol}), incorporating the past studies from literature (Butler, 1993; Butler, Rodono, and Foing, 1988; Thomas and Teske, 1971; Kahler et al., 1982; Butler et al., 1986; Doyle et al., 1988b; Doyle et al., 1988a; Doyle et al., 1991; Johns-Krull et al., 1997). Some of the past reports presented the radiation energy in the Hγ emission ($E_{\mathrm{H}\gamma}$) only and no $E_{\mathrm{H}\alpha}$; then we estimated the latter from the former according to the assumed relation $E_{\mathrm{H}\alpha}$ equals $2 \times E_{\mathrm{H}\gamma}$ in such cases, as Butler (1993) converted the latter to the former using the same conversion factor.

As for the total SXR energy, the flare parameters measured in SXR are converted to those in the bolometric energy band (0.1–100 keV band), using the same method described in **Tsuboi:2016**; the peak bolometric luminosities were obtained, integrating the best-fit spectral parameters with a thin-thermal plasma model for a range of 0.1–100 keV, and then the bolometric X-ray energies E_{Xbol} were calculated from it multiplied by its e-folding times. Table 4.6 summarizes the compiled parameters for the stellar flares. Appendix A gives detailed description about the conversion methods for some of the values in Table 4.6 taken from literature.

Fitting all the data points with a linear model with a slope of unity yields the best-fit relation of

$$\log E_{\mathrm{H}\alpha} = 1 \log E_{\mathrm{Xbol}} - 1.0 \pm 0.7 \ , \tag{4.1}$$

which is shown in Figure 4.5. The error ± 0.7 is calculated as the scatter of the data points around the derived model function in 1.6σ.

Our result finds that the applicable range of the relation extends for further 2 orders in energy: 10^{29}–10^{38} erg. The scattering of the data around the best-fit linear function is limited within an order.

[1] The "integrated flux" with the notations L_X and $L_{\mathrm{H}\gamma}$ in Butler, Rodono, and Foing (1988) and Butler (1993) should be interpreted as, though not explicitly explained in their papers, the radiated energy *integrated over the flare duration*. This means that its dimension is energy (erg), as opposed to the nominally expected units of energy per unit time (erg s^{-1}) for L_*. See the definitions of the parameters in e.g., Thomas and Teske (1971), from which Butler (1993) adopted the values, for verification.

TABLE 4.6: SXR and Hα's radiation energy and e-folding time of large flares

Star	Log ($E_{\rm Xbol}$ [erg])	Log ($E_{\rm H\alpha}$ [erg])	Log ($\tau_{\rm SXR}$ [s])	Log ($\tau_{\rm H\alpha}$ [s])	References
UX Ari	37.1 (36.7–37.5)	36.0 (35.7–36.2)	4.4 (4.1–4.6)	4.91 (4.86–4.98)	This work (Flare 1)
	37.6 (37.3–37.8)	36.3 (35.9–36.5)	4.9 (4.7–5.0)	5.4 (5.3–5.5)	This work (Flare 2)
AR Psc	37.2 (36.7–37.5)	35.5 (35.0–35.9)	4.5 (4.3–4.7)	4.8 (4.6–5.2)	This work (Flare 3)
II Peg	35.6	34.0*	3.6	3.7*	(1), (2)
Gliese 644	33.3	31.8	3.0	3.3	(3)
YZ CMi	31.0	30.0*	2.4	2.0*	(4)
	31.7	31.0*	2.7	2.4*	(5)
UV Cet	29.8	29.0*	2.0	2.4*	(6), (7)
	30.5	29.2*	2.4	2.4*	(6), (7)
	29.8	28.9*	2.4	2.4*	(6), (7)
	30.8	29.6*	3.0	2.7*	(6), (7)
Sun	29.1	28.0	3.3	2.7	(8)
	29.5	28.8	3.3	2.9	(8)
	29.8	29.0	3.3	2.7	(8)
	30.0	29.6	3.6	3.3	(8)
	30.2	29.8	3.6	3.1	(8)
	30.6	30.0	3.6	3.1	(8)
	31.0	30.7	3.9	3.7	(8)
	31.9	30.8	3.9	3.8	(8)
	31.2	29.7	3.5	3.5	(9)

$*$ $E_{\rm H\alpha} = 2 \times E_{H\gamma}$ and $\tau_{\rm H\alpha} = \tau_{\rm H\gamma}$ are assumed.

Note. – The energy band of $E_{\rm Xbol}$ is 0.1–100 keV. The errors indicate the 90%-confidence range. See Appendix B for the detailed method of the calculation.

References: (1)Butler, 1993, (2)Doyle et al., 1991, (3)Doyle et al., 1988b, (4)Doyle et al., 1988a, (5)Kahler et al., 1982, (6)Butler et al., 1986, (7)Butler, Rodono, and Foing, 1988, (8)Thomas and Teske, 1971, (9)Johns-Krull et al., 1997

4.1.6 *e*-folding time

The SXR light curve has limited photon statistics whereas the Hα light curve covers a limited period during each flare (Figure 4.1). Both limitations contribute to the uncertainty in the *e*-folding times that we derived in section 4.1.

As for the SXR, the light curves of some large flares have been shown to contain two components with different *e*-folding times (e.g. Agrawal and Vaidya, 1988; Tsuboi et al., 1998). The decay time of the component that is dominant near the peak is reportedly shorter than the one dominant at the tail. Tsuru et al. (1989) reported re-heating or second flare at the tail of the first and main component in a flare of UX Ari. The decay time that we derived is similar to that of the main flare component ($\sim 6.5 \times 10^4$ s) seen in their lightcurve. Flare 2 might be actually a double flare similar to the one reported by Tsuru et al. (1989), i.e., the SXR light curve of Flare 2 might involve a peak of a possible second flare at around 2 days after the first peak.

With the optical continuum band, intensive studies of flare decay timescales have been made for solar flares. For example, Kashapova et al. (2021) reported two decay components, of which the slower-decay component lasts longer by a factor of 2–10 than the faster-decay one. Our data of Hα covered a small fraction of the flare decay phase, suggesting that we only detected one component out of possibly two or more components in reality in the light curves. Therefore, we conclude that the best-fit *e*-folding times of the SXR and Hα emissions that we measured with the single-exponential model fitting has a (systematic) error of a factor of 2–10 and thus is robust in only one order accuracy.

Many studies of stellar flares (e.g., Kashapova et al., 2021) show that a faster and slower decaying components have a high and low peak fluxes, respectively. Then, the flare energy that is determined from the decay time multiplied by the peak luminosity is not varied much because the uncertainties compensate each other, if to a certain degree.

Veronig et al. (2002b) found a linear correlation between the *e*-folding times $\tau_{\rm SXR}$ and $\tau_{\rm H\alpha}$ for solar flares.

In Figure 4.6, we compiled the same kind of plot, but incorporating the data for stellar flares as in the previous subsection. Here, the reported *e*-folding times were adopted as they are, regardless of the used energy band in each study. The linear relationship is again apparent in this figure. We then fitted the plot with a linear function. The best-fit model, which is overlaid in Figure 4.6, is given by

$$\log \tau_{\rm H\alpha} = 1 \log \tau_{\rm SXR} - 0.1 \pm 0.6 \ , \tag{4.2}$$

where the error is calculated as the scatter of the data points around the derived model function in 1.6σ.

We find that all the data fall within an factor of 4 around the best-fit linear function. This result implies that the two parameters $\tau_{\rm SXR}$ and $\tau_{\rm H\alpha}$ are almost the same among not only the solar flares but also much more energetic stellar flares. The result extends the applicable range for the relationship for an order of magnitude from the previous result (Veronig et al., 2002b). It is notable that the overall trend of the data points in the $\tau_{\rm SXR}$-$\tau_{\rm H\alpha}$ space broadly follows a linear relation for 3 orders of magnitude for the duration τ.

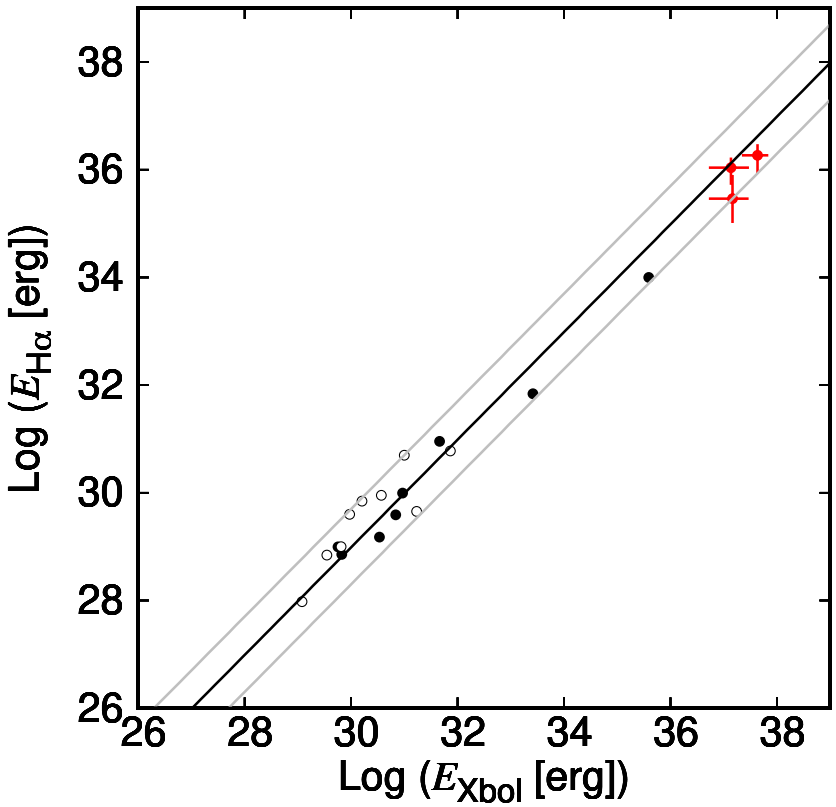

FIGURE 4.5: Log-log plot of radiation energies of Hα and SXR (0.1–100 keV). The open and filled circles in black show the data for the solar and stellar flares found in literature. The red data are our results for the MAXI flares with 90%-confidence errors. See text for details. The gray lines indicate 1.6 times of the standard deviation (90%) of the data points around the model.

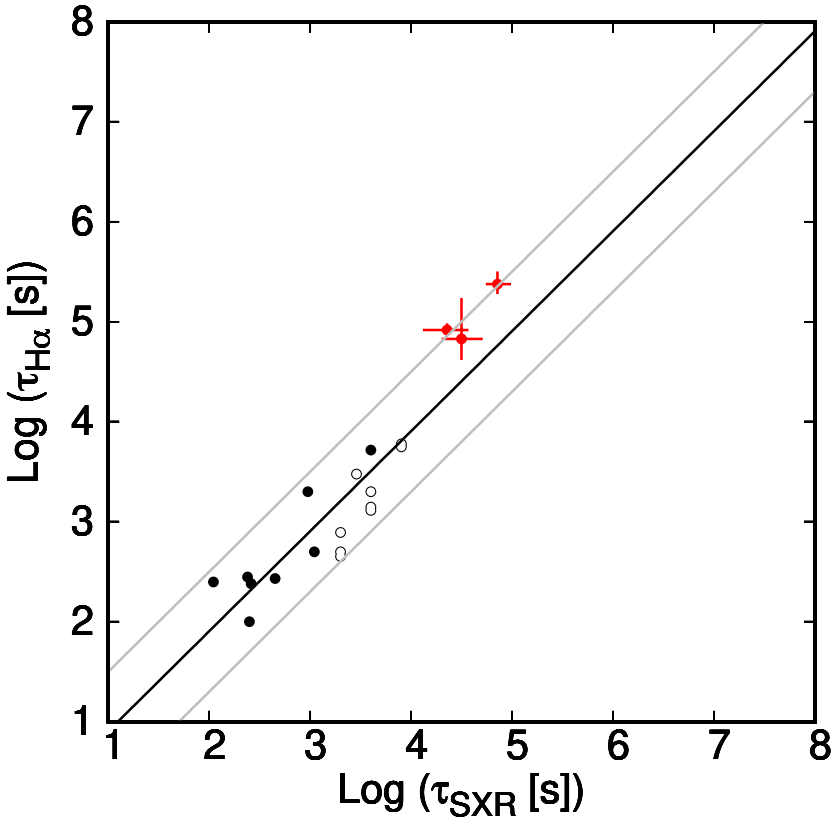

FIGURE 4.6: Log-log plot of *e*-folding times of Hα and SXR. The symbols are the same as in Figure 4.5. The gray lines indicate 1.6 times of the standard deviation (90%) of the data points around the model.

4.2 Discussion

4.2.1 Solar to large stellar flares

We have found proportional relationships between the SXR and Hα emission line for the flare radiation energy E and e-folding time τ from the solar to large stellar flares. As for the Sun, thanks to the close distance to the Sun, many images have been obtained with high spatial resolution in the Hα emission line and SXR band (e.g. Asai et al., 2004; Jing et al., 2016). SXRs are dominated by optically-thin thermal emission from high-temperature plasma of tens of millions of degrees that fills the loop of each flare (e.g. Shibata and Magara, 2011). Hα line is, by contrast, found to be emitted near the foot-points of flare loop and/or from the inner side of SXR flare loop, called postflare loop (see Figure 42 in Shibata and Magara, 2011). The hydrogen responsible for the Hα emission line is thought to be excited by one or all of (1) the collision of accelerated particles, (2) heat conducted from the high-temperature plasma at the foot-point of the flare loop, and (3) the high-energy radiation from the high-temperature plasma. The nominal loop size of the solar flare is reported to be $\sim 0.1\ R_\odot$ (e.g. Kontar, Hannah, and Bian, 2011). Although the loop size of Flares 1 and 2 are estimated to be more than twice of the stellar radius, our finding of the scaling relationships suggests that the origins of the SXR and Hα of the large flare are common to those of the Sun.

In this work, the studied correlation is limited to Hα and X-rays. Although some studies have been done about the correlation between white light and X-rays, the uncertainty in the results is considerable mainly due to their limited radiated-energy ranges of the sample stellar flares (e.g., Flaccomio et al., 2018; Guarcello et al., 2019; Kuznetsov and Kolotkov, 2021). Future simultaneous observations of stellar flares with X-rays and other bands, including white light, would provide us with insights about the multi-wavelength nature of stellar flares for a wide energy band.

4.2.2 Estimation of active area and flare loop position

In this study, I estimated the active regions on the stellar surface using SCAT observations of the Hα line of UX Ari during quiescence, and the flare loop positions of Flare 1 and 2 using visible continuum and radio observations. First, to get the information about the orbital motion of UX Ari, we measured the central wavelength of the Hα emission lines and measured their Doppler shifts. As a result, the modulation in 2016 and 2018 when we observed Flare 1 and 2 show sinusoidal variations in the central wavelengths of the Hα emission lines in accordance with the rotation period, with amplitudes of 120 and 110 km/s in the line-of-sight velocity, respectively (Figures 4.7 and 4.8). The Doppler shift in Hα emission was converted to velocity using the equation $v/c=\Delta\lambda/\lambda$. UX Ari is reported by (Hummel et al., 2017) to emit Hα lines, so the radial velocities observed here are considered to be active regions of the primary star. Comparing this variation with the phase of Hummel et al. (2017), in which the phase of the main star, the quasi-giant star, is set to 0 in front of the companion main-sequence star, the phase shift is about $-0.02 - 0.06$, which is consistent with previous reports. The Doppler shifts at the time of the Flare 1 and 2 events were the same as the Doppler shifts at the same phase in quiescent states, indicating that the Hα emission regions in Flare 1 and 2 are both on the primary side. Since the Hα emission region, which is the foot of the flare loop, was not found on the companion star side.

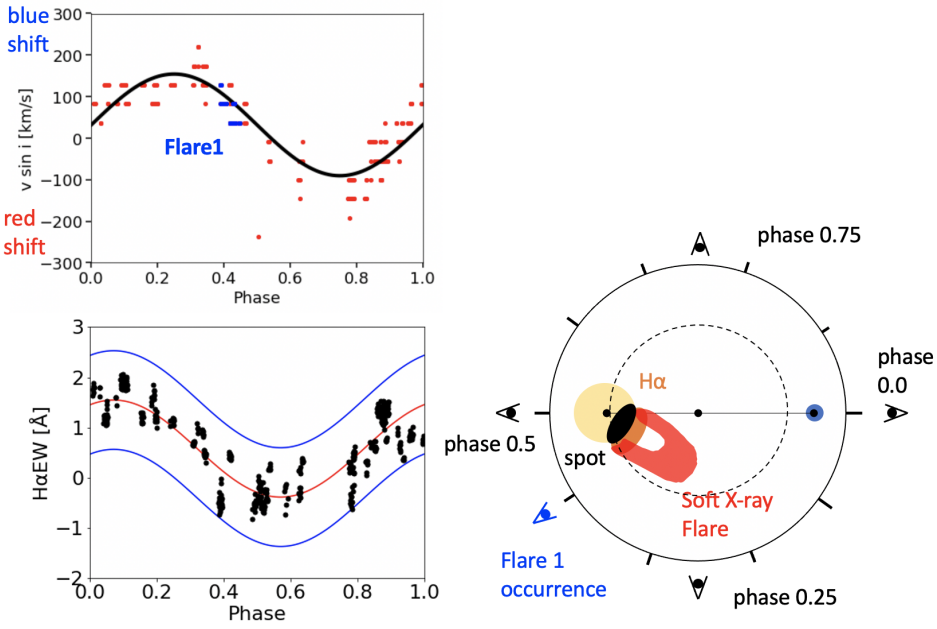

FIGURE 4.7: *Right*: A schematic ilust of UX Ari between October 2016 and March 2017. The yellow and blue circle is the primary (subgiant) and secondary (mainsequence) star. An outer circle is the phase of binary-position seen from the observer. A blue eye-mark is the phase of Flare 1 occurence. A black filled circle and a orange filled circle is spot position and Hα emission region, respectively. A red loop is schematic shape of the flare loop which can seen in soft X-ray. The dashed circle is estimated radii of the Hα component with the radial velocity of 120 km/s. $Upperleft$: A folded curve of the radial velocity. $Lowerleft$: A folded curve of the Hα EW. The folding base date and period are MJD 56237.634 and 6.43788 days, respectively (**Himmel:2017**).

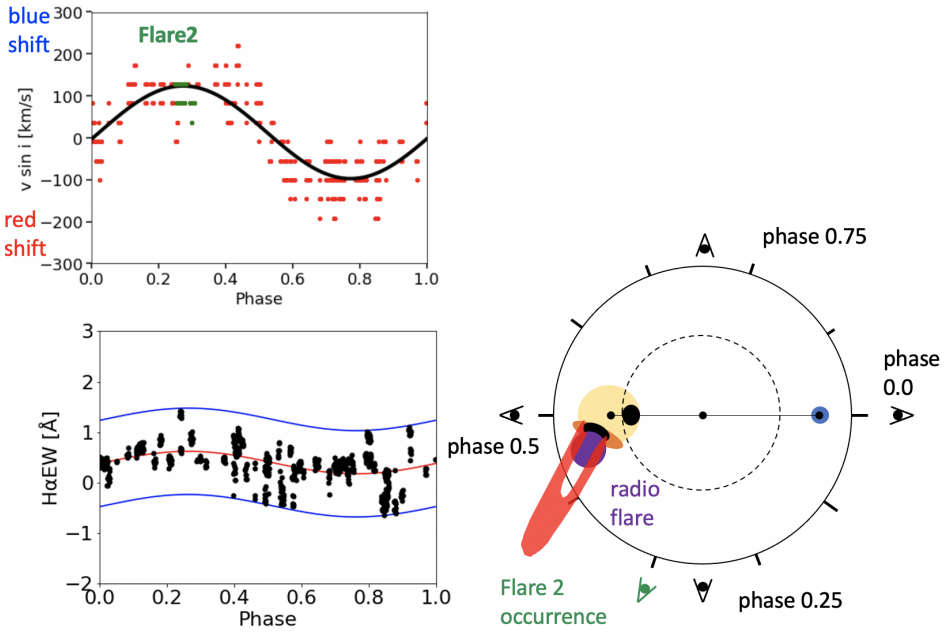

FIGURE 4.8: *Right*: A schematic ilust of UX Ari between October 2018 and March 2019. The symbols are same as Figure 4.7. A purple mark is estimated position of the radio flare. The dashed circle is estimated radii of the Hα component with the radial velocity of 110 km/s. *Upperleft*: A folded curve of the radial velocity. *Lowerleft*: A folded curve of the Hα EW. The folding base date and period are MJD 56237.634 and 6.43788 days, respectively (**Himmel:2017**).

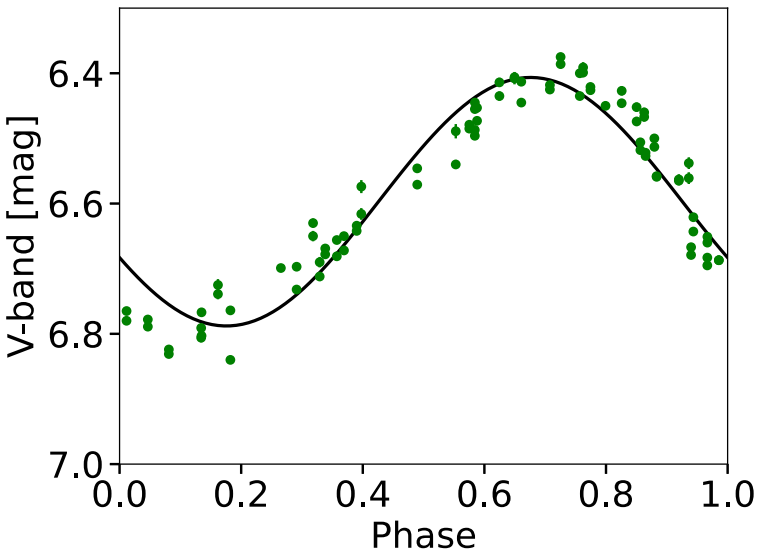

FIGURE 4.9: The folded modulation of V-band magnitude observed by KWS. The solid curve is the best-fit model of the sinusoidal curve.

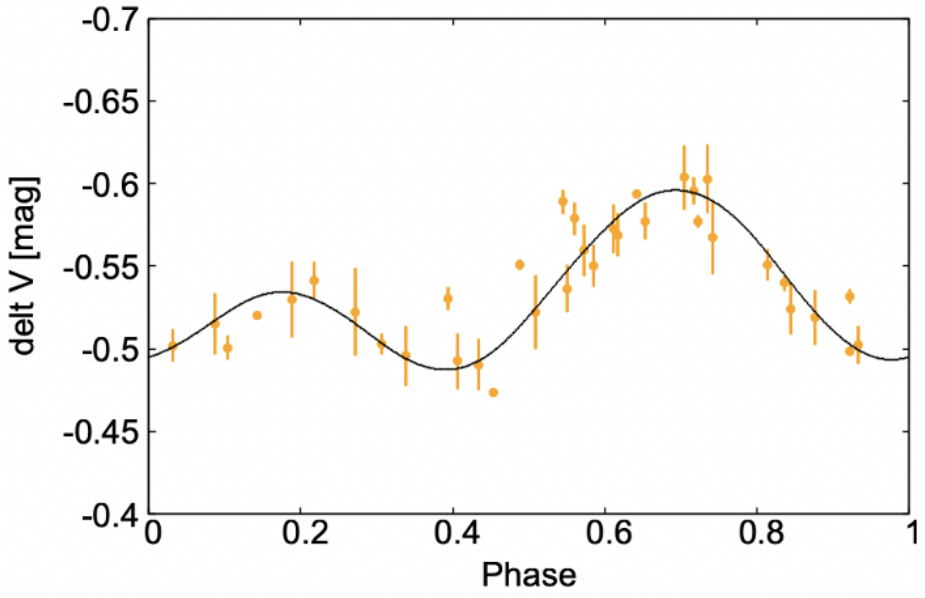

FIGURE 4.10: The folded modulation of V-band magnitude observed by CAT. The solid curve is the model curve calculated by using FHOEBE analysis software.

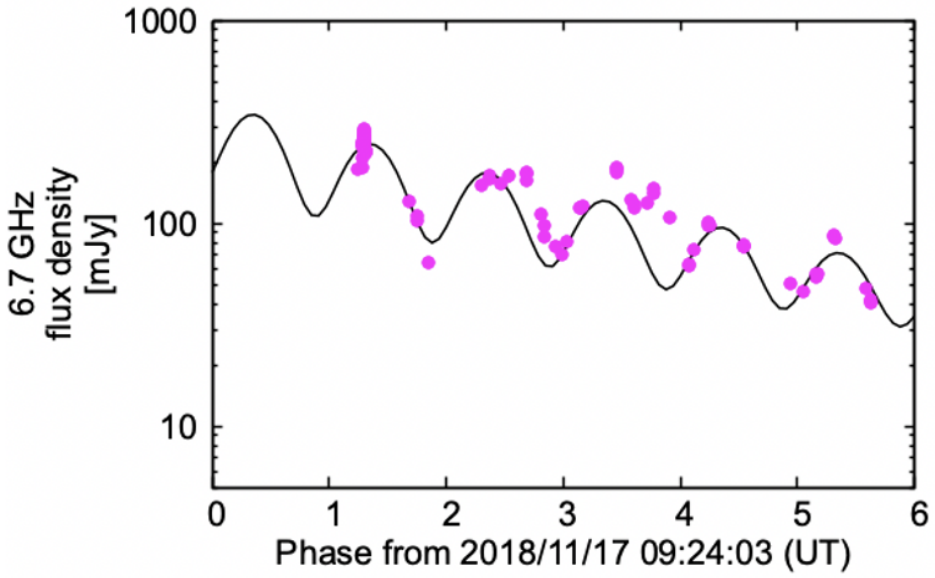

FIGURE 4.11: The light curve of 6.7 GHz radio emission. The solid curve is the best-fit model of the sinusoidal and exponential decay plus constant.

Using the same method as in section4.1.1, we summarized the yearly variations of Hα EW in 2016 and 2018 during quiescence (Figure C.1 and C.4). We were not able to identify the active region in 2018 because the EW fluctuation was small in 2018 while the EW fluctuation was significant in 2016 when Flare1 occurred. We drew a schematic ilusts of the surface of the main star, which was facing the Earth during the phase when Hα EW was brightening, as the surface where the active region exists (Figure 4.7 and 4.8). Flare 1 was occurred in the phase that emits Hα during the quiescent phase based on Doppler shift observations, so we assumed that the flare position was also above the active region during the quiescent phase (Figure X). Flare 1 was occurred at the same location as the Hα emitting component in the quiescent state, based on Doppler shift observations, so we assumed that the flare location was also above the active region in the quiescent state (Figure 4.7).

In addition to SCAT observation, we also used the observations of visible continuum and radio to draw a picture of Flare 1 and 2, including sunspots and flare locations. We used two optical telescope to observe V-band magnitude of the quiescent states in 2016 and 2018. One is KWS, which was installed at Okayama observatory. The results of KWS observations were opened to access. Hence, I referred the results of V-band observation in FY 2016. In order to measure the luminosity variations caused by sunspots, we constructed a light curve folded with the rotation period (Figure 4.9). Since the light curve showed sinusoidal variations, we estimated that the sunspots were located on the surface of the star facing forward in the faintest phase. The position of the sunspot is given by Hα EW. The position of the sunspot is consistent with the Hα emitting region (Figure 4.7). This means that Flare 1 occurred above the sunspot on the primary star, which is consistent with the general picture of a solar flare.

The results of Kitakoga in prep. 2022, which summarizes the observations of the visible light telescope CAT at Chuo University and radio emissions of UX Ari in 2018 including Flare 2 (Figure 4.10). They estimated the position and area of sunspots using FHOEBE analysis software based on the 1-year V-band luminosity variations. We have drawn the estimated sunspot positions in Figure **??**. The estimated sunspot area is 1.5 10^{22} cm^2 on the side close to the phase where the Hα emission region is located. The radio emission of Flare 2 decays with a sinusoidal variation according to the rotation period, and its maximum is around 0.3 phase (Figure 4.11). They attributed this sinusoidal fluctuation to stellar obscuration, and estimated the region of Flare 2's radio emission. We have included the region of radio emission in Figure 4.8. This region is the same location as the sunspots. Similar to Flare 1, if we consider that the Hα emission region at quiescence is above the sunspot, the Hα emission region of Flare 2 is considered to be consistent with the radio emission region and the sunspot. This means that the spatial information of Flare 2 is also similar to that of Flare 1, which is similar to solar flares.

This is the second paper to discuss the location of flare loops in binary stars. The first report was reported by Schmitt and Favata (1999). This is an X-ray observation of a flare in Algol, which is classified as a RS CVn-type star. The observations revealed brief periods of dimming and brightening during the decay in the X-ray luminosity variations, and the timing of the dimming and brightening coincided with the timing of the eclipse of the binary star, leading to an estimate of the flare source. To use the method of this report, the target's inclination must be at a value that causes an eclipse. We used much of the information obtained using multiple wavelengths to discuss the location of the binary flare source. The method we used is a universal method that can be applied to any target. Our results are the first step to prove that this universal method is practical.

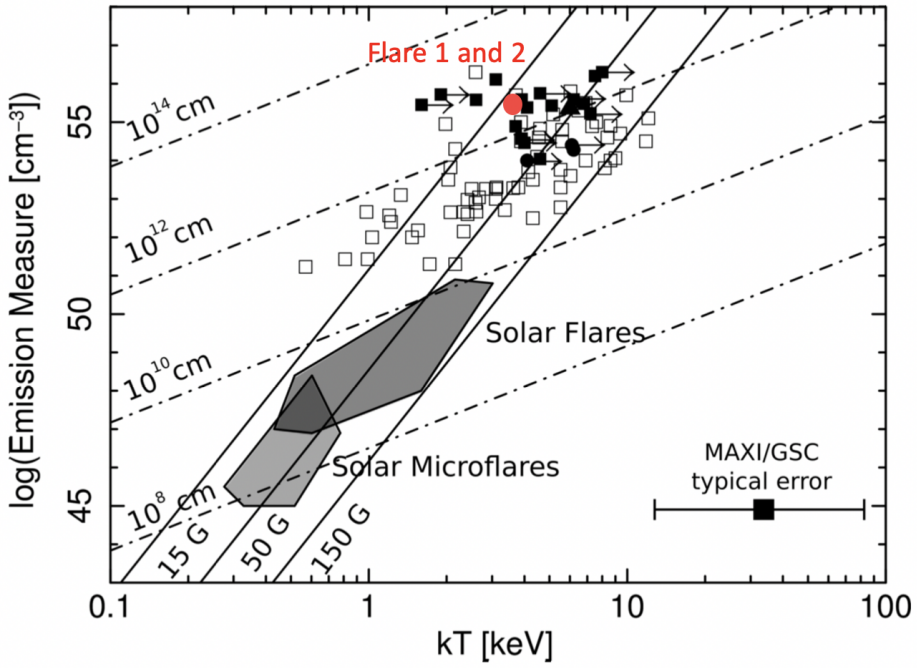

FIGURE 4.12: Universal correlation of emission measure and temperature. The symbols and curves are same as Figure 1.6. The red circle is a plot of Flare 1 and 2.

4.2.3 Evaluation of a model to measure flare loop length

The model used in this study requires the use of the temperature and/or Emission measure (EM) obtained from the X-ray spectral analysis to obtain the flare loop length. However, in the spectral analysis of Flare 1 and 2, the fitting was performed assuming a temperature kT of 3.5. Therefore, the obtained flare loop length is a low confidence value because it assumes not only the model but also the temperature. In order to evaluate the variability of the measured kT and EM, we plotted the fit results of Flare 1 and 2 on the correlation diagram of EM vs kT for stellar flares including the Sun (Figure 4.12). This position is considered to have a 5-fold and 100-fold variation in kT and EM, respectively, compared to the sample of previous studies. This variability can be explained by the fact that the (Shibata and Yokoyama, 1999) and (Haisch, 1983) models change their estimates of the flare loop length by a factor of 100 and several times, respectively. Therefore, in this result, we consider the loop length obtained by the model of (Haisch, 1983), which can be used to obtain more reliable results in the loop length calculation using the model.

Flare 2 was estimated in Kitakoga in prep. 2022 to have a sunspot area of 1.5 10^{23} cm^2 at the foot of the flare loop from the V-band luminosity variation. In order to evaluate whether the cross-sectional area of the flare loop is comparable to this sunspot area, we calculated the cross-sectional area considering the shape of the flare loop assumed in the model. Since the model of (Haisch, 1983) assumed the cross section of the flare loop to be $(L/10)^2$, we estimated the cross section of Flare 2 to be 6×10^{22} cm^2. This is about 0.5 times smaller than the cross section at the sunspot foot, and given the variability in kT and EM, the sunspot area and flare loop cross sections are considered to be consistent. This spatial information is similar to that observed in solar flares, so it is consistent to assume that giant flares are a

scaled-up version of solar flares.

Chapter 5

Summary

1. We launched SCAT, a visible light spectroscopic telescope for the study of stellar flares, in 2016.

2. We evaluated the performance of SCAT and found that it can observe the Hα line (6563 Å) with a wavelength resolution R of 600 and a limiting magnitude of 13 and the accuracy of wavelength determination of $\pm$ 1Å.

3. We have established a system to observe large flares simultaneously with Hα and SXR by using SCAT to follow-up the flares detected by MAXI. Using this system, we obtained the following results.

4. During the five years from 2016 October to 2021 September, three large stellar flares from UX Ari and AR Psc were simultaneously observed in Hα and SXRs.

5. The radiation energies of the observed flares were 10^{36}–10^{37} erg in the SXR band and 10^{35}–10^{36} erg in the Hα emission line. By combining the obtained physical parameters and those in literature for solar and stellar flares, a good proportional relation was obtained between the emitted energies of SXR and Hα emissions for a flare energy range of 10^{24}–10^{38} erg. This is the first confirmation of the relationship based on simultaneous X-ray and Hα observations of massive stellar flares. The ratio of the Hα line emission to that of SXR is about 0.1, if we take the energy band from 0.1 to 100 keV to obtain the X-ray luminosity.

6. The *e*-folding times in the decay phase of SXR and Hα flares were obtained to be both 10^{4}–10^{5} s. By combining the obtained physical parameters and those in literature for solar and stellar flares, it is confirmed that the *e*-folding times in both bands coincide with the range of 1–10^{4} sec.

7. Even very large stellar flares with energies of 6 orders of magnitude larger than the most energetic solar flares follow the same scaling relationships established for solar and much less energetic stellar flares. This fact suggests that their physical parameters can be estimated on the basis of the known physics of solar and stellar flares.

8. Using multi-wavelength observations, we succeeded in inferring the spatial information of giant flares. As a result, we obtained a hint of the spatial information of flares that could connect binary stars.

9. Looking ahead, to put a stronger limit on the size of flare loops, we can make spectroscopic observations with next-generation X-ray telescopes such as XRISM.

Appendix A

Calculation of radiation energies and *e*-folding times from those in literature

The general procedure to calculate the radiation energies and *e*-folding times in SXRs and Hα (tabulated in Table 4.6) is described in Sections 4.1.5 and 4.1.6. In some cases, the values are taken from the cited references as they are presented. However, in many cases, some conversions are required to derive the compiled values (Table 4.6). Here is the detail of the conversion methods. (II Peg) $E_{\rm Xbol}$ is calculated from the peak X-ray flux (referred to as $F_{\rm X,peak}$) and $\tau_{\rm SXR}$, both of which are read directly from a figure in the reference, and $\tau_{H\alpha}$ is read directly from a figure. (Glise 644) $E_{\rm Xbol}$ is calculated in a similar manner as that for II Peg except that $F_{\rm X,peak}$ is taken from a table. (YZ CMi with reference 4 in Table 4.6) $\tau_{\rm SXR}$ is calculated from a combination of $F_{\rm X,peak}$ directly read from a figure and energy in reference (7), and $\tau_{\rm H\alpha}$ is, from the peak Hα flux ($F_{\rm H\alpha,peak}$) from a table and $E_{\rm H\alpha}$ in reference (1). (YZ CMi with reference 5) $\tau_{\rm SXR}$ is from $\tau_{\rm SXR}$ calculated from $F_{\rm X,peak}$ and $E_{\rm X}$ in reference (5), and $\tau_{\rm H\alpha}$ is directly from a figure. (UV Cet) $\tau_{\rm SXR}$ is from $F_{\rm X,peak}$ and $\tau_{\rm SXR}$ directly from a figure, and $\tau_{\rm H\alpha}$ is from a combination of $F_{\rm H\alpha,peak}$ directly from a figure and $E_{\rm H\alpha}$ from reference (1). (Sun with reference 8) $E_{\rm Xbol}$ is from $F_{\rm X,peak}$ directly from a figure, and $\tau_{\rm H\alpha}$ is, in the same manner as that for (UV Cet). (Sun with reference 9) $E_{\rm Xbol}$ is from a combination of $F_{\rm X,peak}$ directly from a figure and $\tau_{\rm SXR}$ from $F_{\rm X,peak}$ and energy from a table.

Appendix B

The results of Monitor observation with SCAT

B.1 Figures

We show the Hα EW light curves obtained by monitor observation with SCAT during September 2016 to April 2021. The sources are RS CVn type stars that can be observed with SCAT.

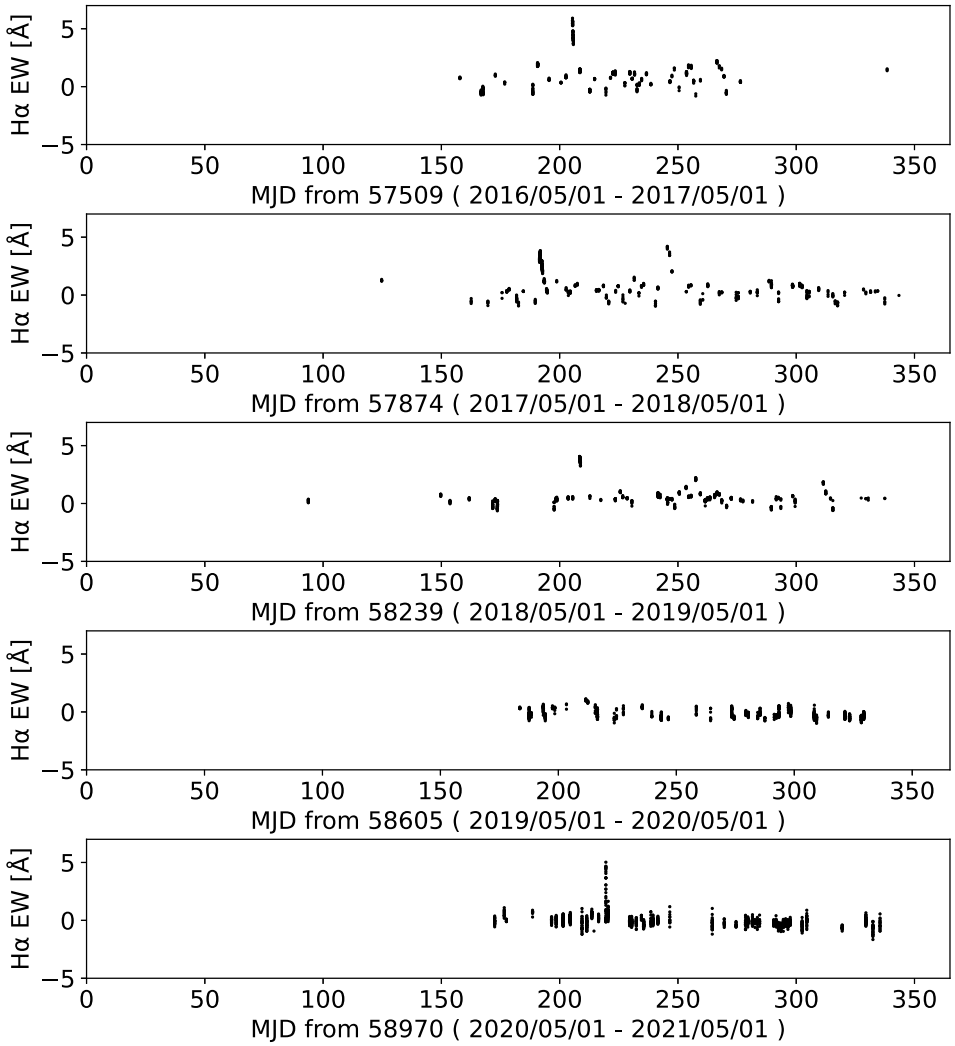

FIGURE B.1: The Hα EW light curves of UX Ari.

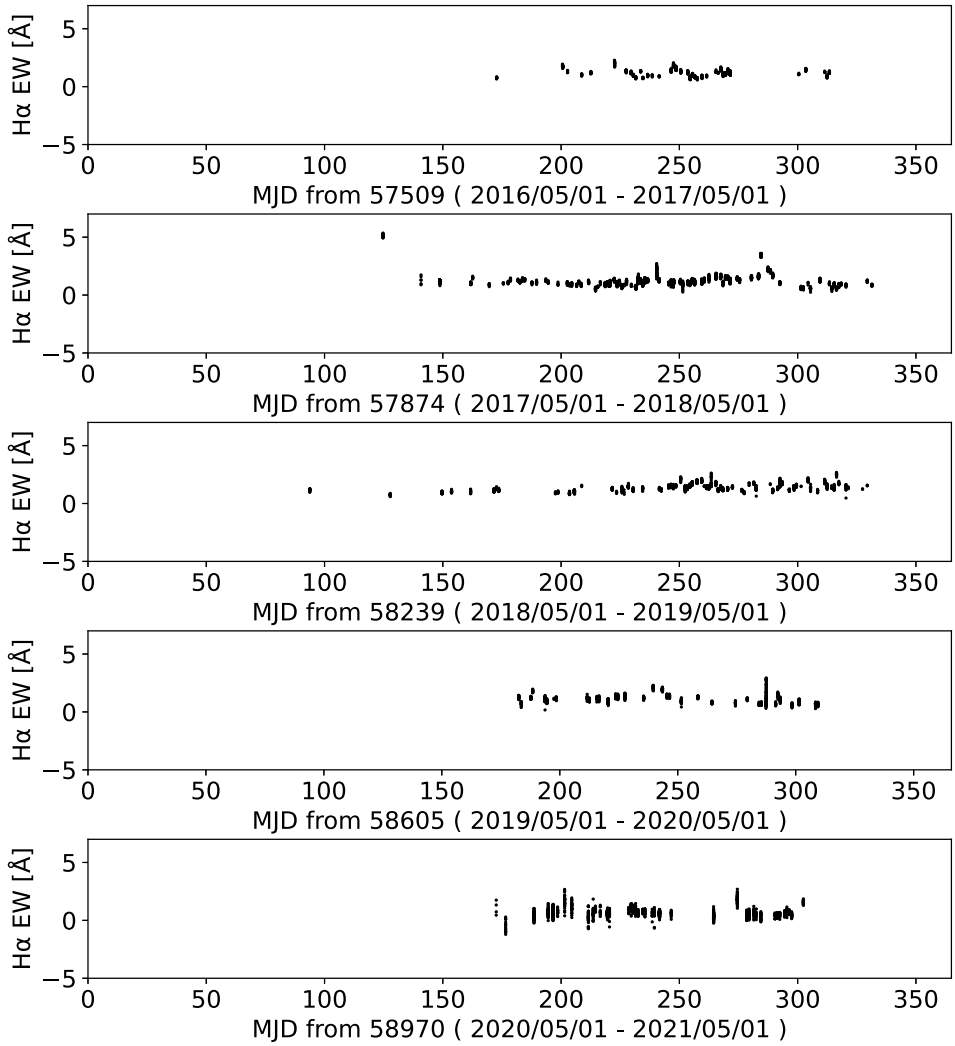

FIGURE B.2: The Hα EW light curves of HR1099.

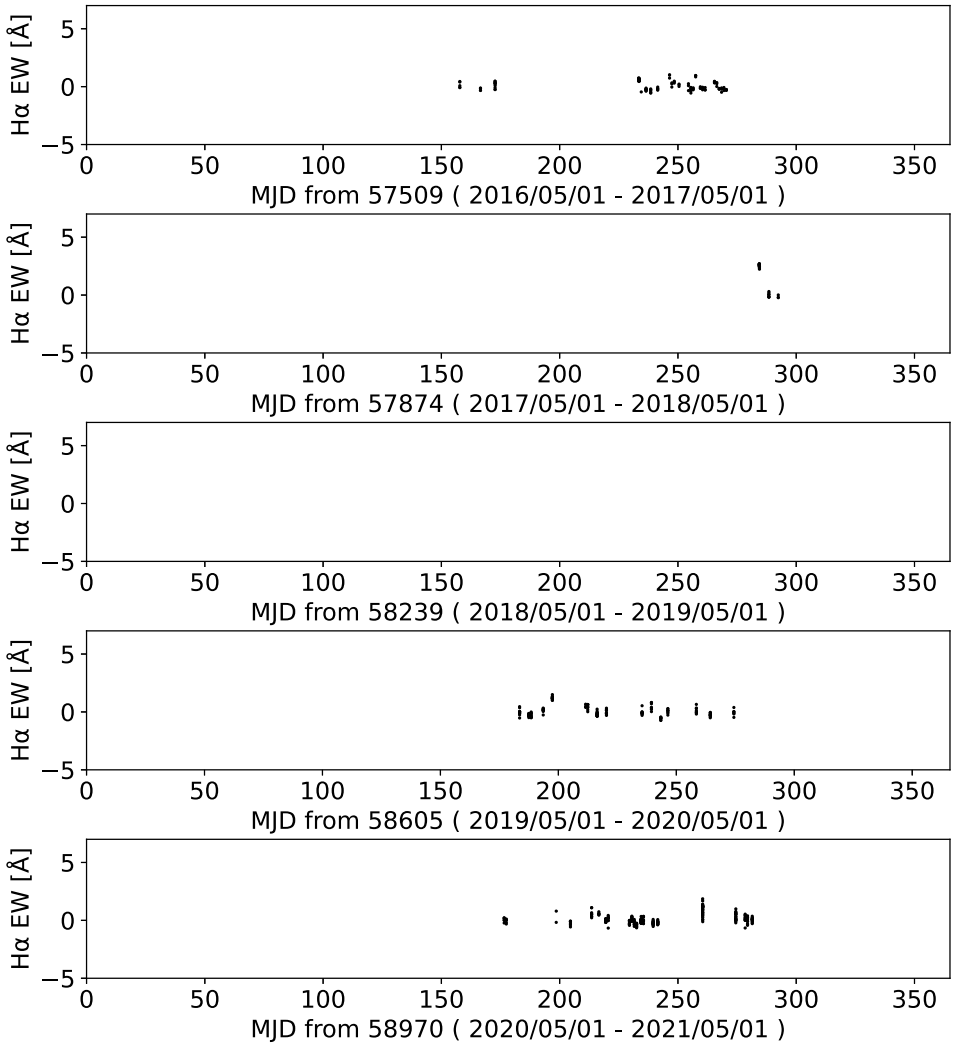

FIGURE B.3: The Hα EW light curves of AR Psc.

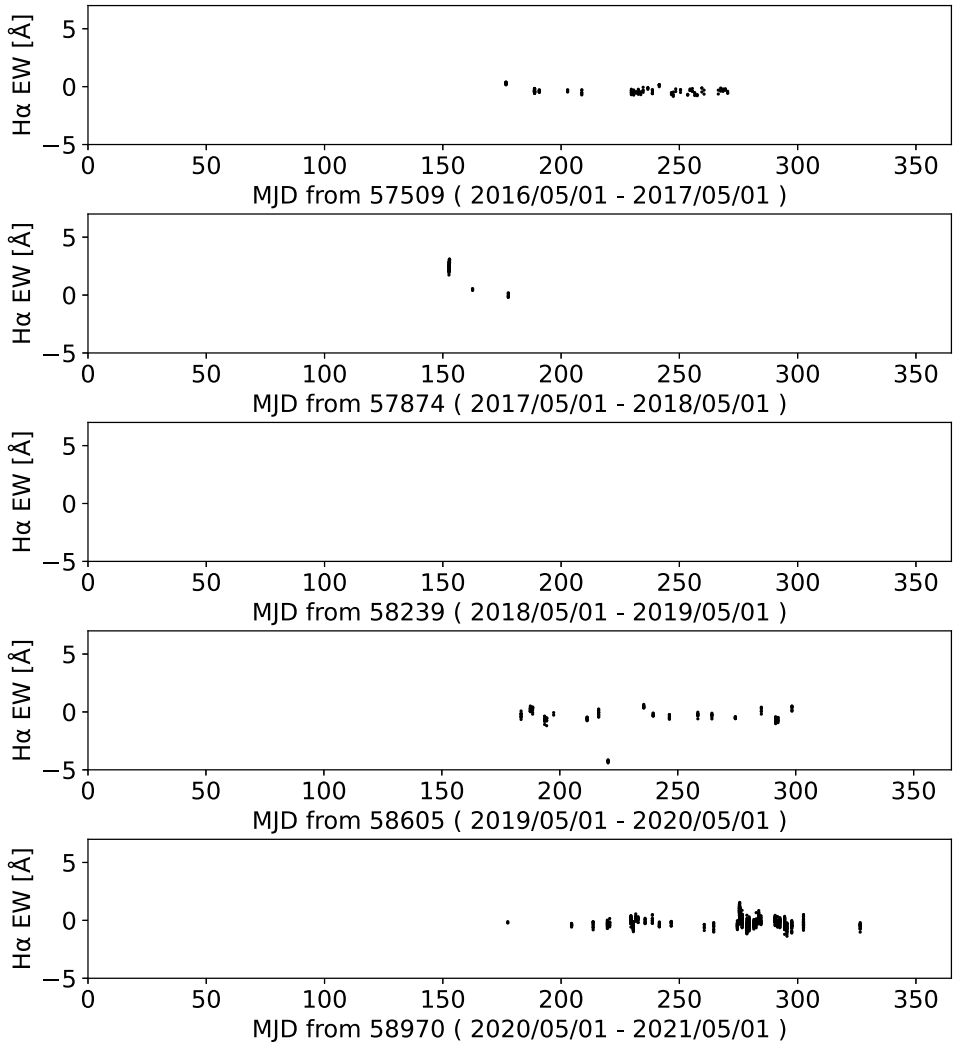

FIGURE B.4: The Hα EW light curves of VY Ari.

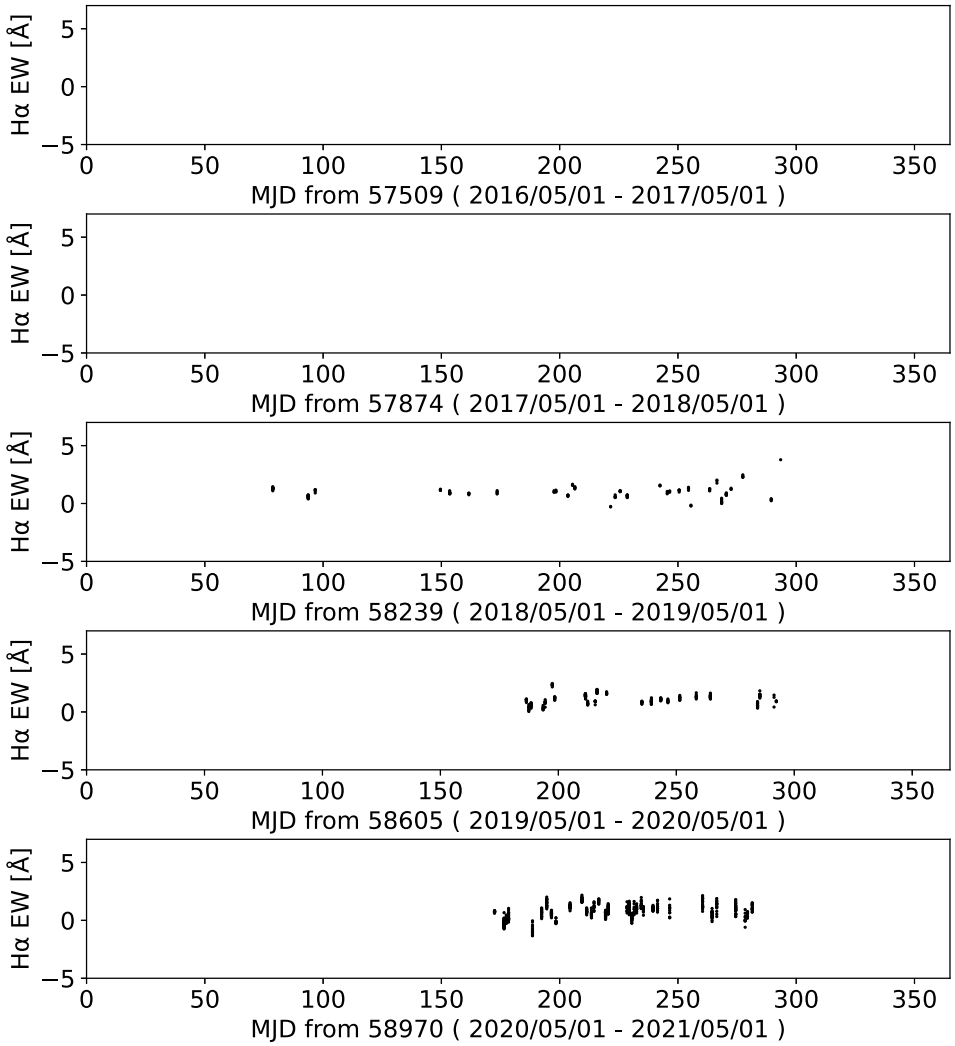

FIGURE B.5: The Hα EW light curves of II Peg.

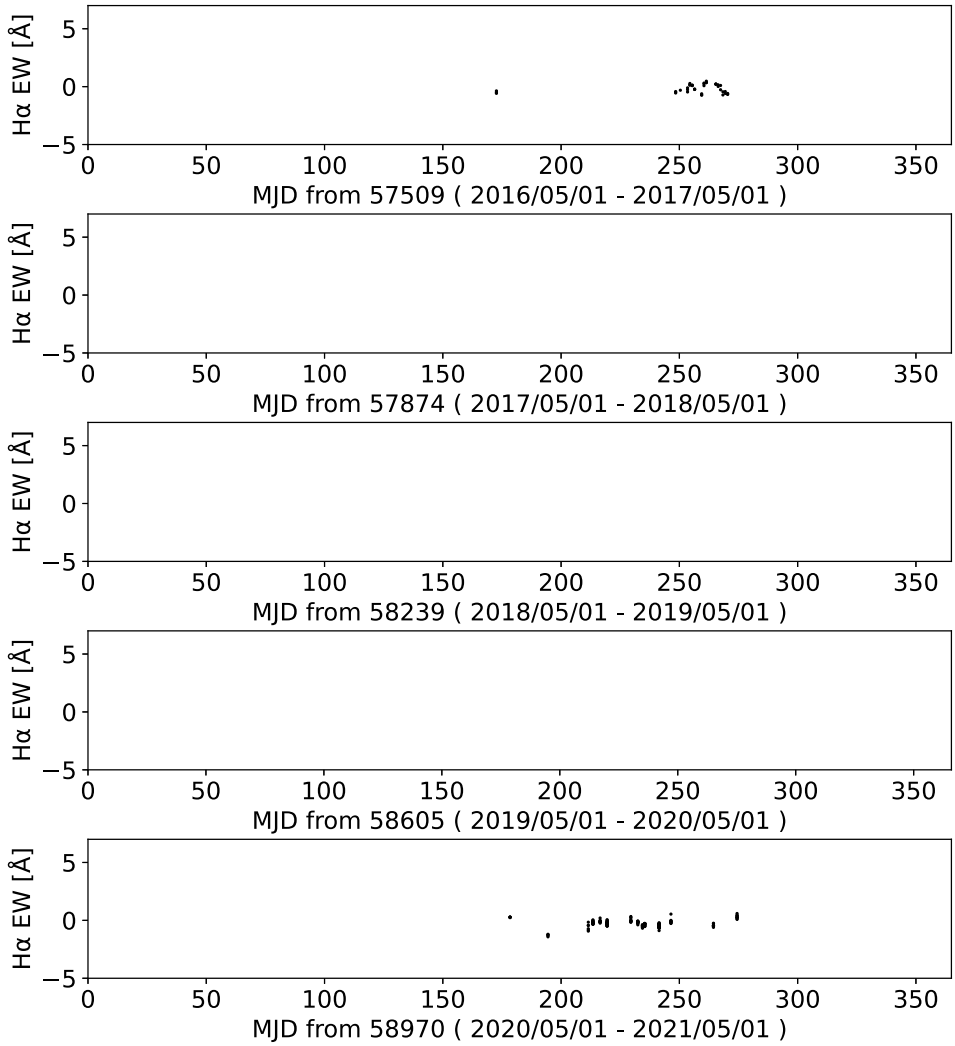

FIGURE B.6: The Hα EW light curves of IM Peg.

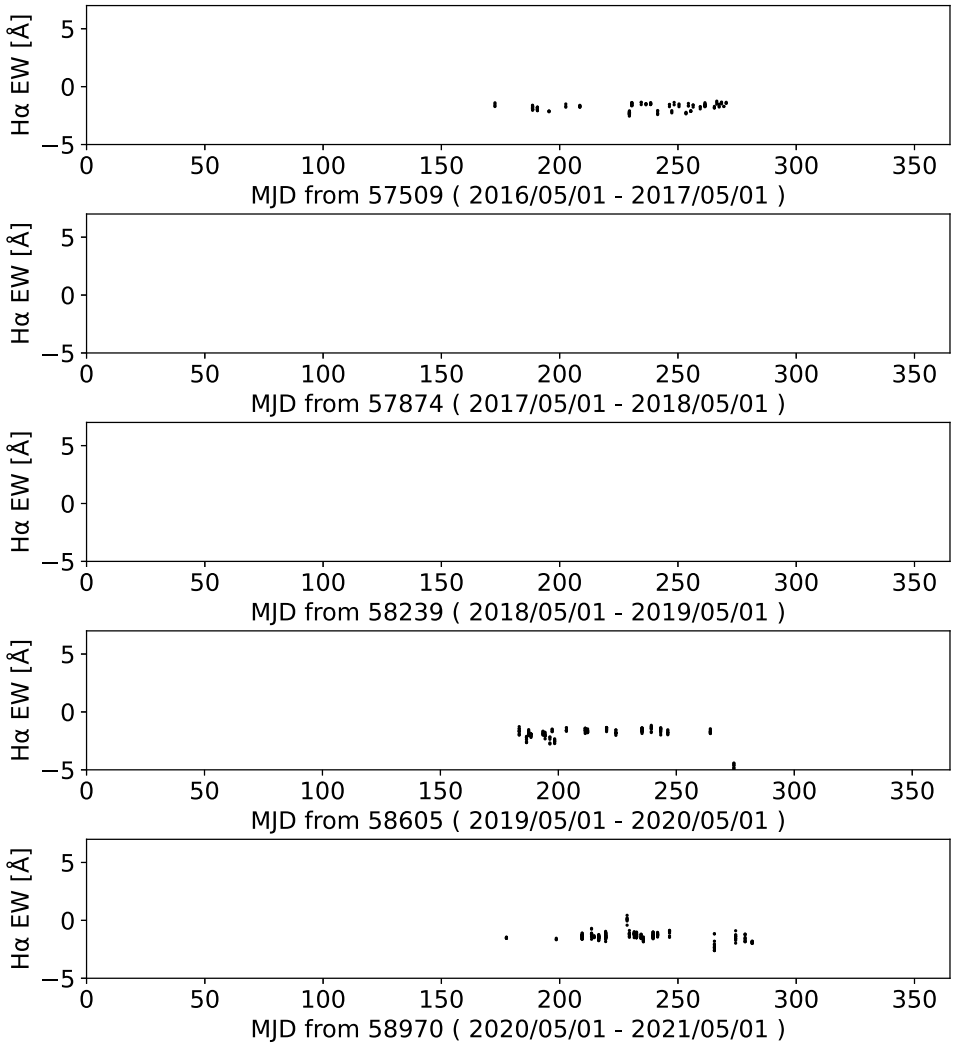

FIGURE B.7: The Hα EW light curves of AR Lac.

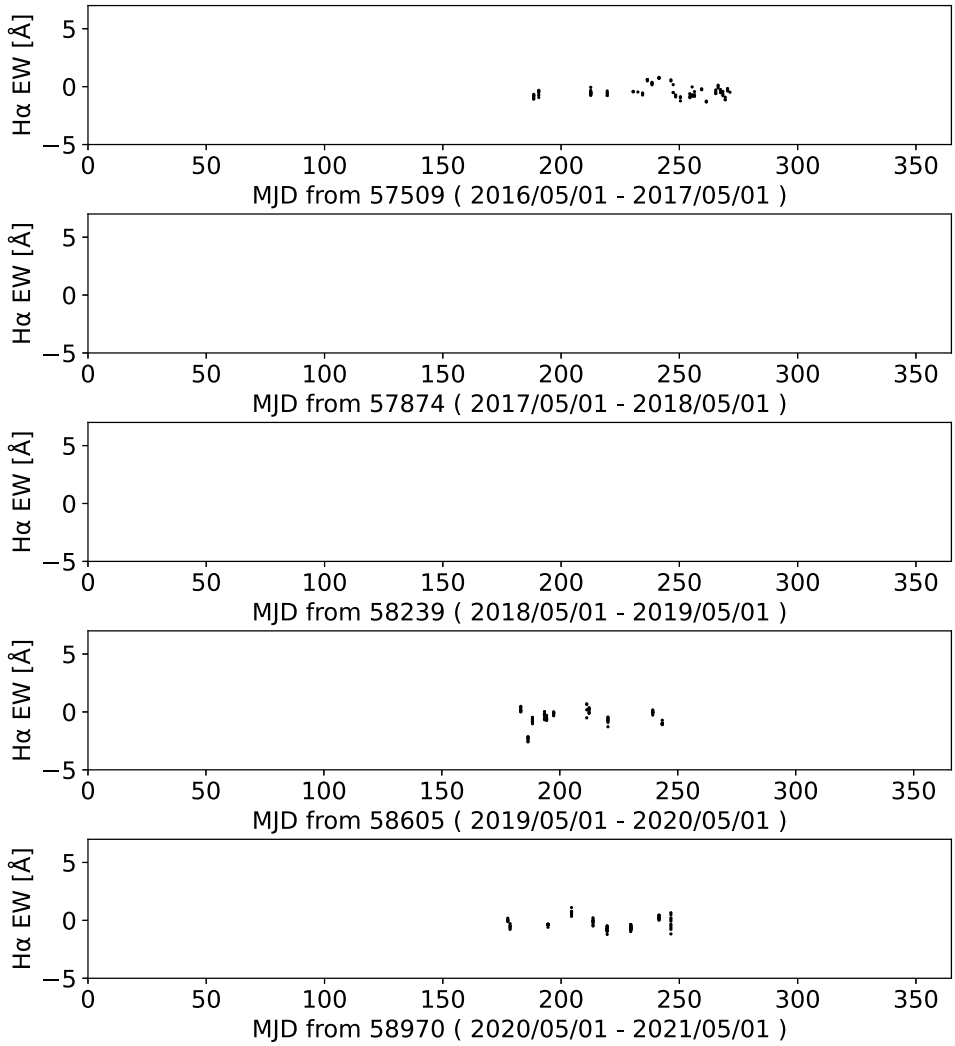

FIGURE B.8: The Hα EW light curves of SZ Psc.

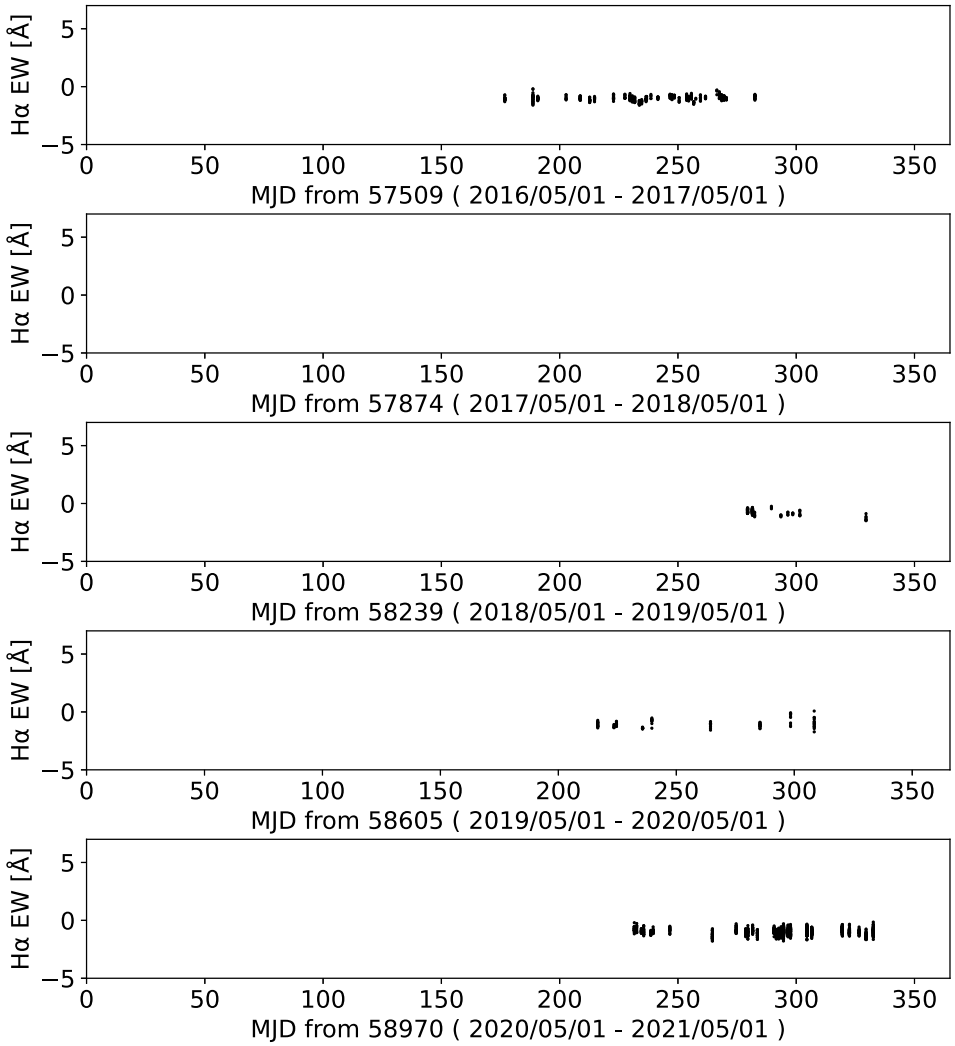

FIGURE B.9: The Hα EW light curves of sigma Gem.

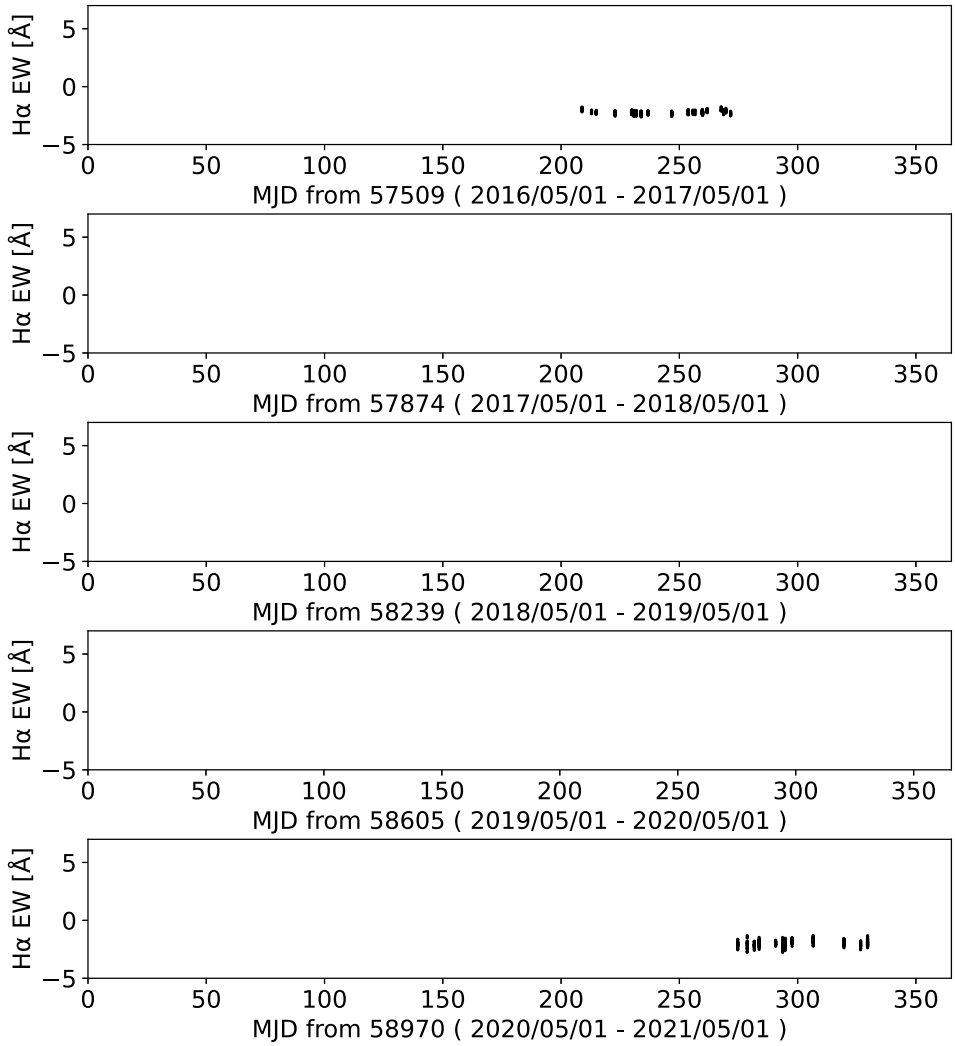

FIGURE B.10: The Hα EW light curves of BH CVn.

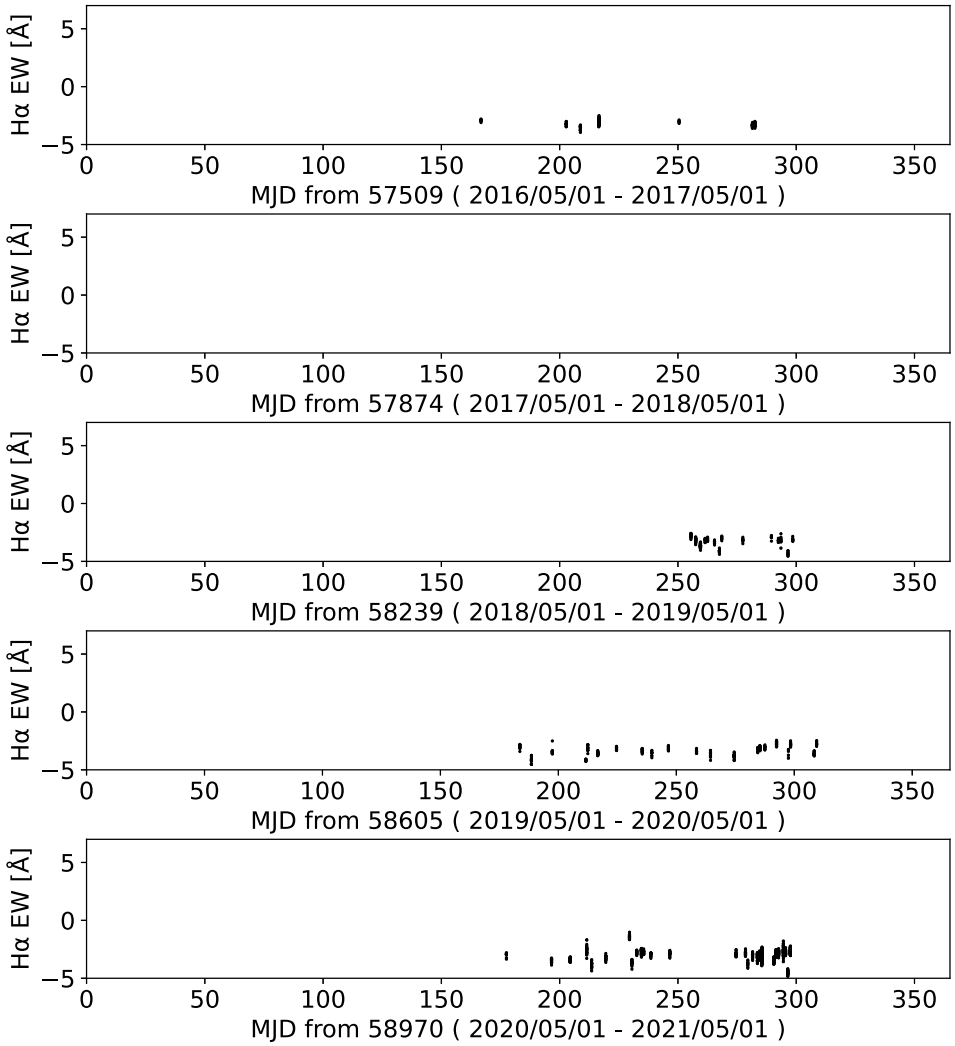

FIGURE B.11: The Hα EW light curves of Algol.

Appendix C

The figures of Hα EW light curves to obtain the persistent EW

C.1 Figures

We show the Hα EW light curves to obtain EW of persistent component from Hα EW light curves of 7 flares.

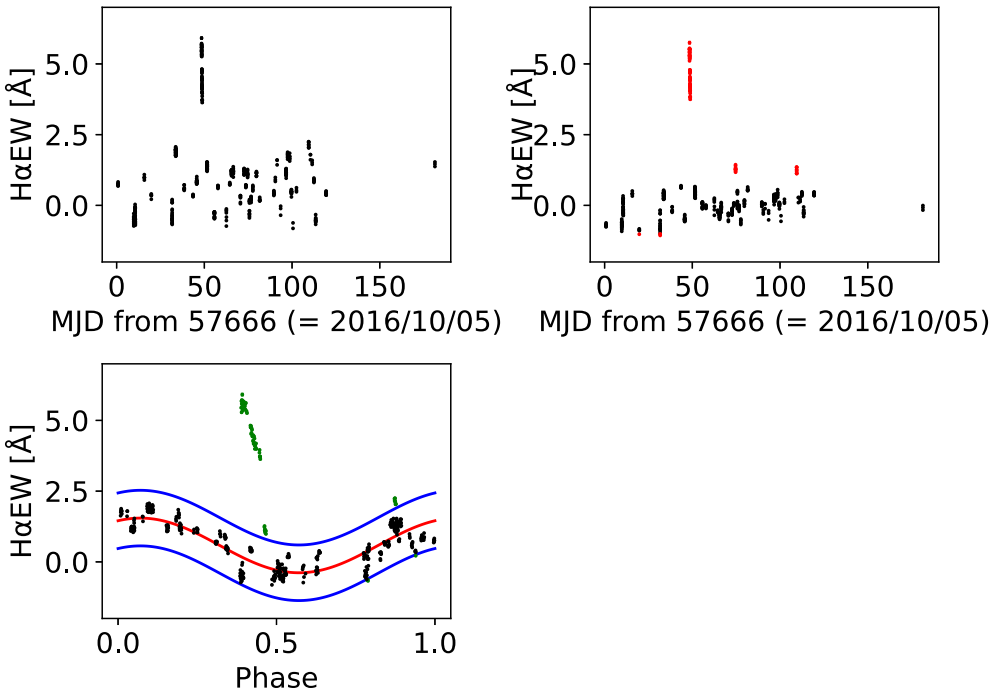

FIGURE C.1: The Hα EW light curves of Flare 1. *Upperleft*: The observed raw Hα EW light curve. *Upperright*: The Hα EW light curve subtracted EW of persistent component. The red plots are excluded plots to fit the quiescent EW. *Lowerleft*: Folded Hα light curve. The red curve is the best fit of the model. The blue curves are the curve obtained by adding $\pm$ 2.5 σ to the best fit parameters. The green plots are the points that were removed when fitting the quiescent component.

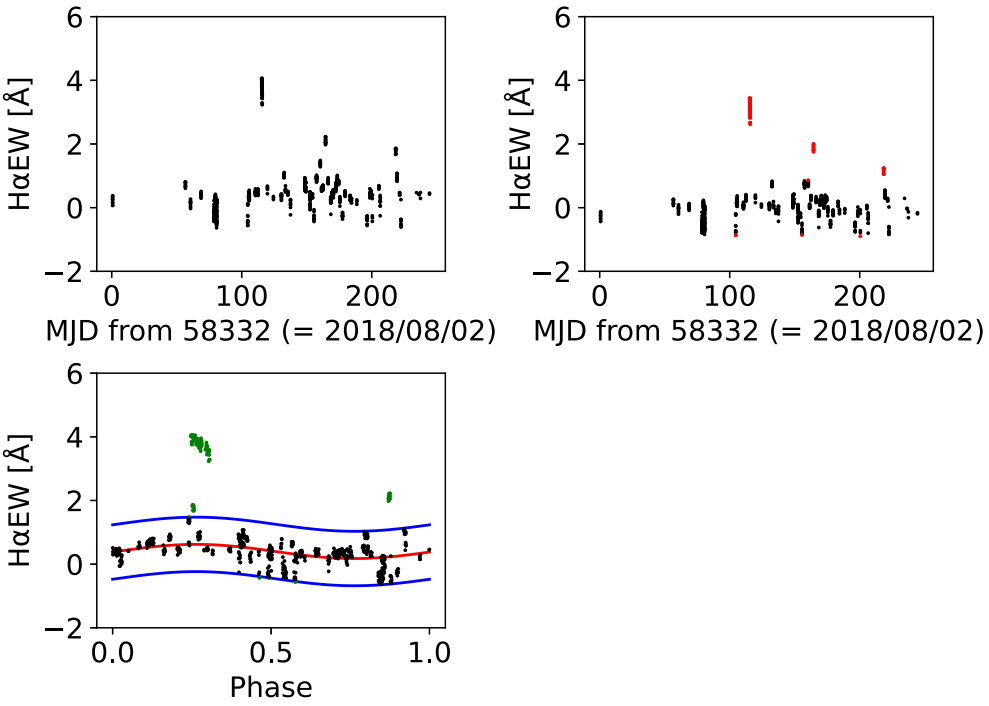

FIGURE C.2: The Hα EW light curves of Flare 2. The symbols and curves shown in three figures are same as Figure C.1

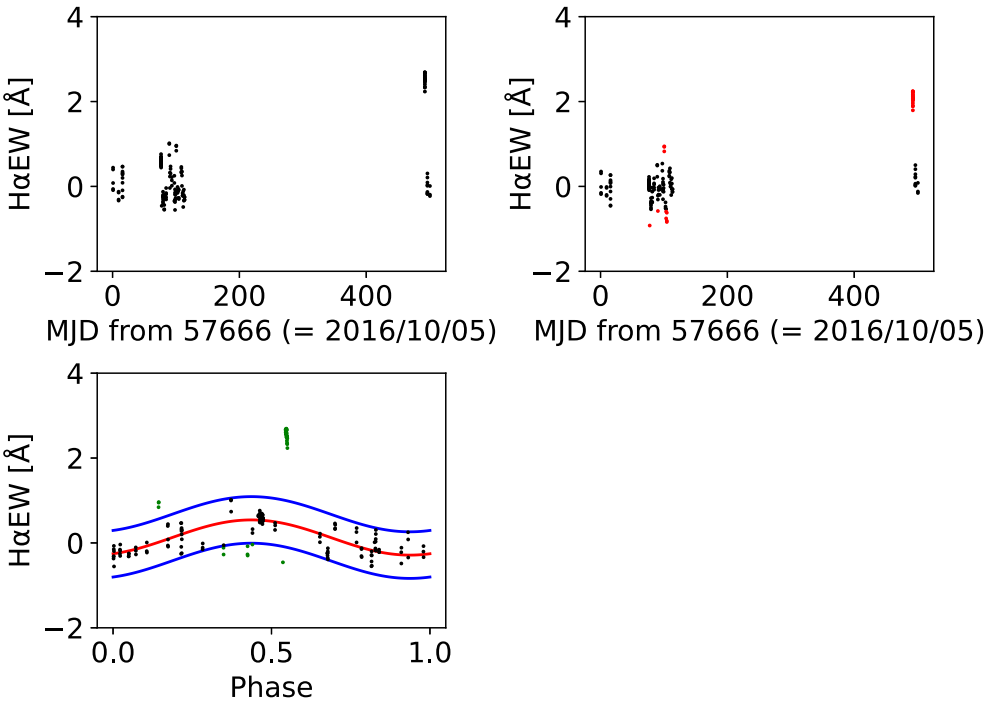

FIGURE C.3: The Hα EW light curves of Flare 3. The symbols and curves shown in three figures are same as Figure C.1

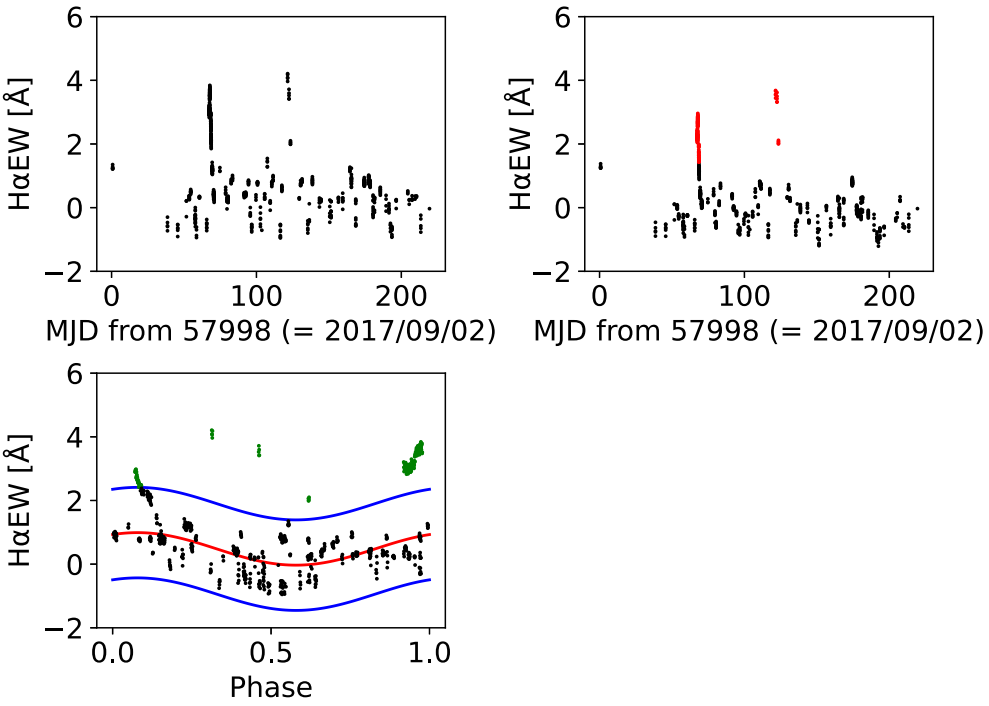

FIGURE C.4: The Hα EW light curves of Flare 4. The symbols and curves shown in three figures are same as Figure C.1

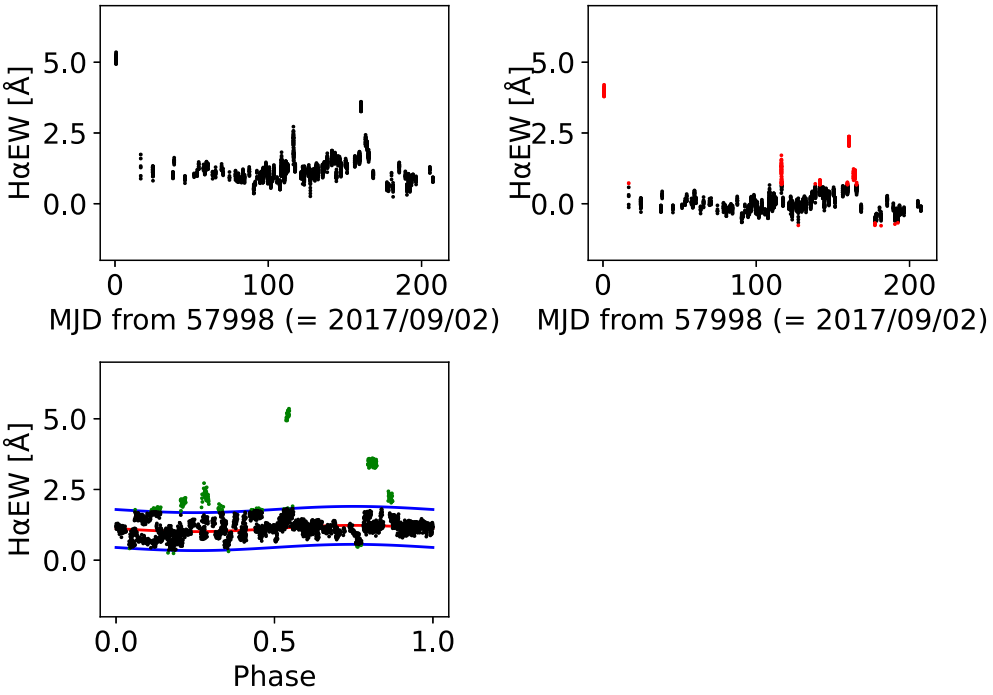

FIGURE C.5: The Hα EW light curves of Flare 5 and 6. The symbols and curves shown in three figures are same as Figure C.1

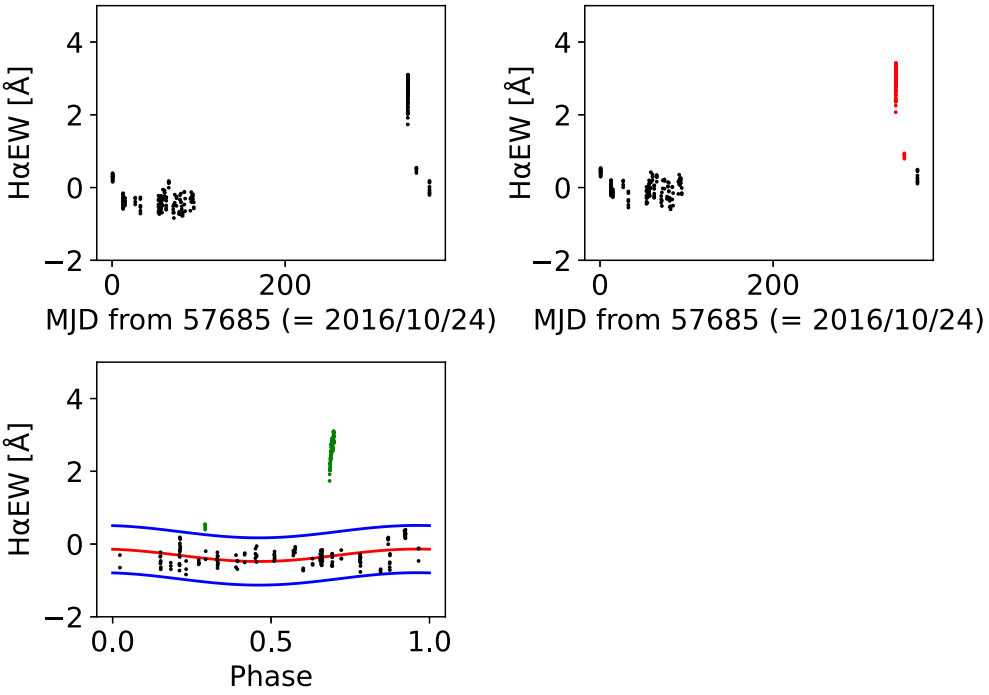

FIGURE C.6: The Hα EW light curves of Flare 7. The symbols and curves shown in three figures are same as Figure C.1

Acknowledgements

First of all, I would like be deeply grateful to my supervisor, Professor Yohko Tsuboi for her continuous advice and kindful support of my study and life. Her insightful advice and encouragement heled me in all time. I am very greatful to Wataru Iwakiri (Chuo University), Yoshitomo Maeda (JAXA/ISAS), Satoru Katsuda (Saitama University) and Yasuharu Sugawara (JAXA/ISAS) for intellectual guidances, comments and discussions.

I would like to appreciate the supports of all people in Chuo University, especially Ryo Sasaki, Tatsuki Sato, Junya Kohara, Sojiro Yamada, Yumiko Nakamura, Yutaka Okamoto, Satoki Kitakoga for their continuous supports.

I would like to appreciate the kindful observations of all people in Chuo University, especially Tatsuru Hirose, Takayoshi Ko, Yuto Ozawa, Emi Minai, Marina Hirano, Yuki Yanagida, Daichi Fukuda, Kyoka Murata, Kenta Oishi, Sota Urabe, Sakura Nawa and Noboru Nemoto for their continuous supports.

Finally, I would like to thank my family for their support.

Publications

Refereed Journal

- **H. Kawai**, Y. Tsuboi, W. Iwakiri et al. (accepted) "X-ray/Hα scaling relationships in stellar flares" 2022, Publications of the Astronomical Society of Japan
- R. Sasaki, Y. Tsuboi, W. Iwakiri, S. Nakahira, Y. Maeda, K. Gendreau, M. F. Corcoran, K. Hamaguchi, Z. Arzoumanian, C. B. Markwardt, T. Enoto, T. Sato, **H. Kawai** et al. "The RS CVn type star GT Mus shows most energetic X-ray flares throughout the 2010s" 2021, The Astrophysical Journal, Volume 910, Issue 1, id.25
- K. Namekata, H. Maehara, R. Sasaki, **H. Kawai** et al. " Optical and X-ray observations of stellar flares on an active M dwarf AD Leonis with the Seimei Telescope, SCAT, NICER, and OISTER" 2020, Publications of the Astronomical Society of Japan, Volume 72, Issue 4, id.68
- B. P. Abbott, R. Abbott, T. D. Abbott, et al. (**H. Kawai** : alphabetical order of 2,506th), "Multi-Messenger Messenger of a Binary Neutron Star Merger" 2017, The Astrophysical Journal Letters, Volume 848, Issue 2, article id. L12, 59 pp. (2017).

International Conferences

- **H. Kawai**, Y. Tsuboi, R. Iizuka, et al. "The extended linear correlation between the Hα and the soft X-ray emissions in the solar and stellar flares」" Helicity Thinkshop 2013, University of Tokyo, Session 4.3, Oral (2017/11)

Bibliography

Agrawal, P. C. and J. Vaidya (Nov. 1988). "Binary phase correlated X-ray intensity variations and flaring in theRS CVn binary HR 1099." In: *MNRAS* 235, p. 239.

Alekseev, I. Y. and O. V. Kozlova (Oct. 2001). "Spots and Active Regions on the Emission-Line Star VY Ari". In: *Ap* 44, p. 429.

Asai, A. et al. (Aug. 2004). "Flare Ribbon Expansion and Energy Release Rate". In: *ApJ* 611, p. 557.

Bopp, B. W. and Jr. Fekel F. (Sept. 1976). "HR 1099: a new bright RS CVn variable." In: *AJ* 81, p. 71.

Butler, C. J. (May 1993). "An extended correlation between the Balmer and soft X-ray emission from solar and stellar flares." In: *A&A* 272, 507, p. 507.

Butler, C. J., M. Rodono, and B. H. Foing (Nov. 1988). "A correlation between Balmer and soft X-ray emission from stellar & solar flares." In: *A&A* 206, L1, p. L1.

Butler, C. J. et al. (1986). "Coordinated Exosat and spectroscopic observations of flare stars and coronal heating". In: *Nature* 321, 679, p. 679.

Carlos, R. C. and D. M. Popper (Aug. 1971). "HD 21242, A Spectroscopic Binary with H and K Emission". In: *PASP* 83, 494, p. 504.

Catalano, S. et al. (Oct. 2003). "A Simultaneous H α and Radio Flare on the RS CVn System UX Ari". In: *in Cambridge Workshop on Cool Stars, Stellar Systems, and the Sun, 12, The Future of Cool-Star Astrophysics, eds*, p. 981.

Doyle, J. G. et al. (Mar. 1988a). "Rotational modulation and flares on RS CVn and BY DRA systems. VII. simultaneous X-ray, radio and optical data for the dMe star YZ CMi on 4/5 March 1985." In: *A&A* 193, 229, p. 229.

Doyle, J. G. et al. (Feb. 1988b). "Rotational modulation and flares on RS CVn and BY DRA systems. VIII. Simultaneous EXOSAT and H alpha observations of a flare on the dMe star GL 644 AB (Wolf 630) on 24/25 August 1985." In: *A&A* 191, 79, p. 79.

Doyle, J. G. et al. (Feb. 1991). "Simultaneous detection of a large flare in the X-ray and optical regions on the RS CVn-type star II Peg." In: *MNRAS* 248, 503, p. 503.

ESA (1997). "The HIPPARCOS and TYCHO catalogues. Astrometric and photometric star catalogues derived from the ESA HIPPARCOS Space Astrometry Mission". In: *ESA Special Publication, 1200*.

Fekel, F. C. (1996). "Chromospherically Active Stars. XV. HD 8357=AR Piscium, an Extremely Active RS CVn System". In: *AJ* 112, p. 269.

Fekel, F. C., T. J. Moffett, and G. W. Henry (Feb. 1986). "A Survey of Chromospherically Active Stars". In: *ApJS* 60, p. 551.

Feldman, P. A. (Mar. 1978). "Large Radio Flares in RS CVn Binaries". In: *BAAS* 10, p. 418.

Flaccomio, E. et al. (Nov. 2018). "A multi-wavelength view of magnetic flaring from PMS stars". In: *A&A* 620, p. 55.

Fuhrmeister, B. et al. (Oct. 2011). "Multi-wavelength observations of Proxima Centauri". In: *A&A* 534, p. 133.

Garcia, M. et al. (Sept. 1980). "Optical identification of H 0123+07.5 and 4U 1137-65 : hard X-ray emission from RS CVn systems." In: *ApJ* Vol. 240, p. 107.

Guarcello, M. G. et al. (Feb. 2019). "Simultaneous Kepler/K2 and XMM-Newton observations of superflares in the Pleiades". In: *A&A* 622, p. 210.

Haisch, B. M. (1983). "X-ray observations of stellar flares". In: *in IAU Colloq. 71, Activity in Red-Dwarf Stars, ed. P. B. Byrne & M. Rodono (Dordrecht: Reidel)*.

Hummel, C. A. et al. (Aug. 2017). "Orbital Elements and Stellar Parameters of the Active Binary UX Arietis". In: *ApJ* 844, 115, p. 115.

Jing, J. et al. (Apr. 2016). "Unprecedented Fine Structure of a Solar Flare Revealed by the 1.6m New Solar Telescope". In: *NatSR* 6, p. 24319.

Johns-Krull, C. M. et al. (Sept. 1997). "Hamilton Echelle Spectroscopy of the 1993 March 6 Solar Flare". In: *ApJS* 112, 221, p. 221.

Kahler, S. et al. (Jan. 1982). "Coordinated X-ray, optical and radio observations of flaring activityon YZ Canis Minoris." In: *ApJ* 252, 239, p. 239.

Kanetou, S. et al. (July 2015). "MAXI/GSC detection of a bright X-ray flare from an RS CVn star VY Ari". In: *ATel* 7839.

Kashapova, L. K. et al. (Apr. 2021). "The morphology of average solar flare time profiles from observations of the Sun's lower atmosphere". In: *MNRAS* 502, p. 3922.

Kashyap, V. and J. J. Drake (Oct. 1999). "On X-Ray Variability in Active Binary Stars". In: *ApJ* 524, Issue 2, pp. 988–999.

Kawagoe, A. et al. (2014). "MAXI/GSC detection of a big flare from UX Ari". In: *ATel* 6315.

Kawai, H. et al. (Sept. 2017). "MAXI/GSC detection of a possible X-ray flare from HR1099 (V711 Tau)". In: *ATel* 10753.

Kontar, E. P., I. G. Hannah, and N. H. Bian (Apr. 2011). "Acceleration, Magnetic Fluctuations, and Cross-field Transport of Energetic Electrons in a Solar Flare Loop". In: *ApJL* 730, p. 22.

Kuznetsov, Alexey A. and Dmitrii Y. Kolotkov (Feb. 2021). "Stellar Superflares Observed Simultaneously with Kepler and XMM-Newton". In: *ApJ* 912, p. 81.

Massi, M. and E. Ros (2002). "Investigation of magnetic loop structures in the corona of UX Arietis". In: *6th European VLBI Network Symposium on New Developments in VLBI Science and Technology*, p. 275.

Massi, M. et al. (Apr. 1998). "Activity cycles in UX ARIETIS". In: *A&A* 332, 149, p. 149.

Massi, M. et al. (May 2005). "Discovery of Solar Rieger periodicities in another star". In: *A&A* 435, Issue 1, May III 2005, p. 1.

Matsumura, T. et al. (Apr. 2011). "MAXI/GSC detection of an active state of the RS CVn type star UX Ari". In: *ATel* 3308.

Matsuoka, M. et al. (Oct. 2009). "The MAXI Mission on the ISS: Science and Instruments for Monitoring All-Sky X-Ray Images". In: *PASJ* 61, p. 999.

Mihara, T. et al. (Nov. 2011). "Gas Slit Camera (GSC) onboard MAXI on ISS". In: *PASJ* 63, pp. 623–634.

Nakahira, S., K. Ebisawa, and H. Negoro (Mar. 2013). "Development of the MAXI/GSC all-sky data archive system". In: *JAXA Research and development report: Journal of Space Science Informatics Japan* 2, p. 29.

Nakamura, Y. et al. (July 2016). "MAXI/GSC detection of a possible X-ray flare from an RS CVn star AR Psc". In: *ATel* 9288.

Namekata, K. et al. (Aug. 2020). "Optical and X-ray observations of stellar flares on an active M dwarf AD Leonis with the Seimei Telescope, SCAT, NICER, and OISTER". In: *PASJ* 72, p. 68.

Negoro, H. et al. (2016). "The MAXI/GSC Nova-Alert System and results of its first 68 months". In: *PASJ* 68, S1, p. 1.

Peterson, W. M. et al. (Aug. 2011). "Radio Astrometry of the Triple Systems Algol and UX Arietis". In: *ApJ* 737, Issue 2, article id. P. 104.

Sasaki, R. et al. (Apr. 2017). "A Correlation on Stellar Flares detected with MAXI Quiescent Luminosity vs. Flare Energy ". In: *The X-ray Universe 2017, Proceedings of the conference held 6-9 June, 2017 in Rome, Italy. Edited by J.-U. Ness and S. Migliari.* 201.

Sasaki, R. et al. (Mar. 2021). "The RS CVn-type Star GT Mus Shows Most Energetic X-Ray Flares Throughout the 2010s". In: *ApJ* 910, 25, p. 25. DOI: 10.3847/1538-4357/abde38. arXiv: 2103.16822 [astro-ph.HE].

Schmitt, J. H. M. M. and F. Favata (Sept. 1999). "Continuous heating of a giant X-ray flare on Algol". In: 401.6748, pp. 44–46. DOI: 10.1038/43389. arXiv: astro-ph/9909040 [astro-ph].

Shan, H., X. Liu, and S. Gu (Jan. 2006). "The atmospheric parameters, abundances and magnetic field of the AR piscium primary". In: *New Astron.* 11, 4, pp. 287–292.

Shibata, K. and T. Magara (Dec. 2011). "Solar Flares: Magnetohydrodynamic Processes". In: *Living Rev. Sol. Phys.* 8, 6, p. 6.

Shibata, K. and T. Yokoyama (Nov. 1999). "Origin of the Universal Correlation between the Flare Temperature and the Emission Measure for Solar and Stellar Flares". In: *ApJ* 526, Issue 1, p. L49.

Smith, R. K. et al. (Aug. 2001). "Collisional Plasma Models with APEC/APED: Emission-Line Diagnostics of Hydrogen-like and Helium-like Ions". In: *ApJ* 556, p. 91. eprint: astro-ph/0106478.

Strassmeier, K. G. and B. W. Bopp (June 1992). "Time-series photometric SPOT modeling. I. Parameter study and applicationto HD 17433 = VY Arietis." In: *A&A* 259, p. 183.

Suzuki, M. et al. (Jan. 2010). "MAXI/GSC detection of a flare from HR 1099 (V711 Tau)". In: *ATel* 2401.

Svestka, Z. (1976). "Solar Flares". In: *Physics & Astronomy*.

Thomas, R. J. and R. G. Teske (Feb. 1971). "Solar Soft X-Rays and Solar Activity. II: Soft X-Ray Emission during Solar Flares". In: *Sol. Phys.* 16, 431, p. 431.

Tsuboi, Y. et al. (Aug. 1998). "ASCA Detection of a Superhot 100 Million K X-Ray Flare on the Weak-Lined T Tauri Star V773 Tauri". In: *ApJ* 503, p. 894.

Tsuboi, Y. et al. (Oct. 2016). "Large X-ray flares on stars detected with MAXI/GSC: A universal correlation between the duration of a flare and its X-ray luminosity". In: *PASJ* 68, 90, p. 90. DOI: 10.1093/pasj/psw081. arXiv: 1609.01925 [astro-ph.HE].

Tsuru, T. et al. (1989). "X-ray and radio observations of flares from the RS Canum Venaticorum system UX Arietis." In: *PASJ* 41, 679, p. 679.

Uchida, Y. and T. Sakurai (Jan. 1985). "Magnetodynamical processes in interacting magnetospheres of RS CVn binaries". In: *Unstable Current Systems and Plasma Instabilities in Astrophysics*. Ed. by M. R. Kundu and G. D. Holman. Vol. 107, pp. 281–285.

Veronig, A. et al. (Aug. 2002a). "Relative timing of solar flares observed at different wavelengths". In: *Sol. Phys.* 208, p. 297.

Veronig, A. et al. (Mar. 2002b). "Temporal characteristics of solar soft X-ray and H α flares". In: *Proceedings of the Second Solar Cycle and Space Weather Euroconference* 477, 187, p. 187.

Webb, N. A. et al. (2020). "The XMM-Newton serendipitous survey. IX. The fourth XMM-Newton serendipitous source catalogue". In: *A&A*.

Yokoyama, T. and K. Shibata (Jan. 1998). "MHD Simulation of Chromospheric Evaporation in a Solar Flare Based on Magnetic Reconnection Model". In: *The Hot Universe*. Ed. by Katsuji Koyama, Shunji Kitamoto, and Masayuki Itoh. Vol. 188, p. 213.